CZECH TECHNICAL UNIVERSITY IN PRAGUE

FACULTY OF ELECTRICAL ENGINEERING

Department of Radio Engineering

Testování SpacePix detektoru na podmínky vesmírného prostředí

Environmental testing of the SpacePix pixel detector

Diploma thesis

Study programme:	Aerospace Engineering
Specialization:	Avionics
Author of the thesis:	Bc. Aleš Hrudička
Supervisor:	Ing. Martin Urban

Prague 2019

ZADÁNÍ DIPLOMOVÉ PRÁCE

I. OSOBNÍ A STUDIJNÍ ÚDAJE

Příjmení: **Hrudička** Jméno: **Aleš** Osobní číslo: **434197**

Fakulta/ústav: **Fakulta elektrotechnická**

Zadávající katedra/ústav: **Katedra měření**

Studijní program: **Letectví a kosmonautika**

Studijní obor: **Avionika**

II. ÚDAJE K DIPLOMOVÉ PRÁCI

Název diplomové práce:

Testování SpacePix detektoru na podmínky vesmírného prostředí

Název diplomové práce anglicky:

Environmental Testing of the SpacePix Pixel Detector

Pokyny pro vypracování:

1. Study and describe the importance of dosimetry in space applications both for human crew and hardware components.
2. Study and compare different techniques/detectors for radiation detection.
3. Specify necessary hardware characteristics for space applications regarding space environment.
4. Make a review of methods and suggest an applicable testing procedure for thermal and vacuum testing of the detector.
5. Design (SW and HW) and perform environmental tests after consultation with the supervisor.
6. Evaluate and comment outcomes of the testing and suggest further steps.

Seznam doporučené literatury:

[1] TOWNSEND, Lawrence W.: Implications of the space radiation environment for human exploration in deep space. Radiation protection dosimetry, 2005, 115.1-4: 44-50.
[2] MAURER, R., et al.: RHarsh Environments: Space Radiation. Johns Hopkins APL technical digest, 2008, 28.1: 17.
[3] BENTON, E. R.; BENTON, E. V.: Space radiation dosimetry in low-Earth orbit and beyond. Nuclear Instruments and Methods in Physics Research Section B: Beam Interactions with Materials and Atoms, 2001, 184.1-2: 255-294.
[4] LUTZ, Gerhard, et al: Semiconductor radiation detectors. Berlin: Springer, 1999.
[5] HANDBOOK, ESA Thermal design handbook. ESA, December, 2011.

Jméno a pracoviště vedoucí(ho) diplomové práce:

Ing. Martin Urban, katedra radioelektroniky FEL

Jméno a pracoviště druhé(ho) vedoucí(ho) nebo konzultanta(ky) diplomové práce:

Datum zadání diplomové práce: **10.01.2019** Termín odevzdání diplomové práce: **24.05.2019**

Platnost zadání diplomové práce:
do konce letního semestru 2019/2020

Ing. Martin Urban podpis vedoucí(ho) práce	podpis vedoucí(ho) ústavu/katedry	prof. Ing. Pavel Ripka, CSc. podpis děkana(ky)

III. PŘEVZETÍ ZADÁNÍ

Diplomant bere na vědomí, že je povinen vypracovat diplomovou práci samostatně, bez cizí pomoci, s výjimkou poskytnutých konzultací. Seznam použité literatury, jiných pramenů a jmen konzultantů je třeba uvést v diplomové práci.

. Datum převzetí zadání

Podpis studenta

Statutory declaration

I declare that I have developed and written the enclosed thesis completely by myself, I have not used sources or means without declaration in the text and I have satisfied the ethical principles regarding the development of academic theses, i.e. “Metodický pokyn č.1/2009”.

Prague 24.05.2019 ……

Bc. Aleš Hrudička

Acknowledgments

My great thanks belong to my supervisor Ing. Martin Urban for overall leadership during the completion of this thesis.

ABSTRAKT

Testování SpacePix detektoru na podmínky vesmírného prostředí:

Tato práce se zabývá testováním SpacePix detektoru na podmínky vesmírného prostředí skrze termální cyklování ve vakuu. První část obsahuje popis důležitosti dozimetrických měření ve vesmírných aplikacích. Následuje popis a porovnání historických a aktuálních dozimetrických metod a rozbor nezbytné hardwarové charakteristiky plynoucí z použití techniky ve vesmírném prostředí. V dalších částech práce jsou popsány metody a výsledky testování. Poslední část se věnuje vyhodnocení výsledků a návrhům navazujícího testování.

Klíčová slova:

SpacePix, XChip, vesmírné prostředí, ionizující radiace, efekty ionizující radiace, dosimetrie, pozičně-senzitivní polovodičový detektor, pixelový detektor, radiation hardness assurance, termální cyklování

ABSTRACT

Environmental testing of the SpacePix pixel detector:

This thesis deals with environmental testing of the SpacePix pixel detector through thermal cycling in vacuum conditions. The first part describes the importance of dosimetry in space applications. Afterwards, historical and current dosimetry techniques are introduced and compared. Consequently, the necessary hardware characteristics for space applications regarding the space environment are detailed. In the next parts, the methods for environmental testing and the results of the testing are described. Finally, the outcome is evaluated, and further steps are suggested.

Keywords:

SpacePix, XChip, space environment, ionizing radiation, effects of ionizing radiation, dosimetry, position-sensitive semiconductor detector, pixel detector, radiation hardness assurance, thermal cycling

Contents

List of figures ..... **VIII**

List of tables ..... **X**

List of symbols ..... **XII**

Abbreviations ..... **XIV**

1 Introduction **1**

2 Ionizing radiation **3**

2.1 Alpha particles 3

2.2 Beta particles 4

2.3 Interactions of beta particles 5

2.4 Gamma rays 6

2.5 Interactions of gamma rays 7

3 Ionizing radiation in space **9**

3.1 Galactic cosmic rays 9

3.2 The solar wind and solar particle events 10

3.3 Trapped radiation - Van Allen belts 11

4 Effects of ionizing radiation on electronic hardware components **13**

4.1 Total ionizing dose effects 13

4.2 Single event effects 14

4.3 Displacement damage effects 15

5 Effects of ionizing radiation on humans **17**

6 Ionizing radiation detection techniques **21**

6.1 Gas-filled detectors 22

6.1.1 Ionization chambers 23

6.1.2 Proportional counters 24

6.1.3 Geiger-Müller counters 25

6.2 Scintillation detectors 26

6.3 Semiconductor detectors 28

6.4 Position-sensitive semiconductor detectors 32

6.4.1 Medipix family of pixel detectors 34

6.4.2 The SpacePix pixel detector 35

6.4.3 The XChip pixel detector 37

7 Necessary hardware characteristics for space applications regarding the space environment 39

7.1 The space environment and mitigation strategies 39

7.2 Mitigation of hazard to electronics induced by ionizing radiation 43

7.2.1 Defining the radiation environment 44

7.2.2 Defining the part's failure level 48

7.2.3 Techniques for the increase of radiation tolerance 49

7.2.4 The disadvantages of radiation hardening and the use of COTS components 52

8 Environmental testing methods 55

8.1 TMP100 and TMP461 vacuum-compatibility test 55

8.1.1 Common PCB design 55

8.1.2 Software design 56

8.1.3 Experiment design 58

8.2 Environmental testing of the XChip pixel detector 59

8.2.1 Communication and data log 60

8.2.2 Thermal cycling design 60

8.2.3 Experiment setup 62

9 Results 65

9.1 TMP100 and TMP461 vacuum-compatibility testing 65

9.2 XChip environmental testing 66

10 Conclusion 71

10.1 TMP100 and TMP461 vacuum-compatibility testing 71

10.2 XChip environmental testing 71

10.3 Further steps and suggestions 73

11 References: 75

List of figures

Figure 1: Measured energy resulted from alpha decay. 4
Figure 2: Energy distribution of chlorine-36. 5
Figure 3: Gamma-ray spectrum resulted from gamma decay. 6
Figure 4: A demonstration of three separate regions of dominant interactions. 8
Figure 5: Elemental abundances of GCR for ions from He to Ni. 10
Figure 6: Comparison of solar proton fluences. 11
Figure 7: The proton and electron flux over the South Atlantic. 12
Figure 8: The Van Allen radiation belts. 12
Figure 9: The dependency of the radiation intensity on the thickness of a shield. 14
Figure 10: SEU recorded by the UOSAT-3. 15
Figure 11: Radiation-induced degradation of solar cells. 16
Figure 12: A microscopic view of an Ilford G.5 nuclear emulsion. 17
Figure 13: The energy and flux of cosmic radiation. 21
Figure 14: The dependency of ion-electron pairs production on the applied voltage. .. 23
Figure 15: Schematic illustration of ionization chamber. 24
Figure 16: Schematic illustration of proportional counter. 25
Figure 17: The Geiger plateau curve. 26
Figure 18: Schematic illustration of a photomultiplier tube. 27
Figure 19: The crystal lattice structure of undoped silicon. 28
Figure 20: The crystal lattice structure of Si containing P impurities. 29
Figure 21: The crystal lattice structure of Si containing B impurities. 29
Figure 22: A schematic diagram of P-N junction. 30
Figure 23: Comparison of germanium detector and scintillation detector. 32
Figure 24: Schematic illustration of a hybrid pixel cell. 33
Figure 25: A schematic diagram of the Timepix modes. 34
Figure 26: A reconstruction of an image recorded by the Timepix. 35
Figure 27: The transfer function of individual pixels of the SpacePix detector 36
Figure 28: The XChip pixel detector bonded to a PCB. 38
Figure 29: Degradation of solar panels caused by atomic oxygen 40
Figure 30: Degradation of the Optical Properties Monitor caused by UV radiation. .. 41
Figure 31: Outcomes of the ISS Material experiment 4. 42
Figure 32: TID at the centre of a solid aluminium sphere 46
Figure 33*: Integral LET spectra in 1 AU distance.* 47
Figure 34: The offset voltage of PM155 as a function of the total dose. 49

Figure 35: Enclosed layout transistor and guard ring configurations. 51
Figure 36: A schematic diagram of TMP100 and TMP461 common PCB. 56
Figure 37: A PCB diagram of TMP100 and TMP461 common PCB. 56
Figure 38: A sample of the code used for TMP100 and TMP461 measurement. 57
Figure 39: Completed test setup on top of the cold plate. 58
Figure 40: Temperature oscillations on a base plate of a LEO spacecraft. 61
Figure 41: Illustration of the M-pattern of the thermal cycle design. 61
Figure 42: An example of a step-like layout of the thermal cycle. 62
Figure 43: The XChip test setup. 63
Figure 44: The results from testing TMP100 and TMP461. 65
Figure 45: Images reconstructed from XChip 1, XChip 2 measurements. 66
Figure 46: Histograms reconstructed from XChip 1, XChip 2 measurements. 67
Figure 47: The total energy deposited as a function of temperature. 68
Figure 48: The mean energy deposited as a function of temperature. 68
Figure 49: The standard deviation as a function of temperature. 69
Figure 50: The bottom detection limit as a function of temperature. 70

List of tables

Table 1: Exposure levels for an example of reference missions. 18
Table 2: Effective dose limits for a 1-year mission. 19
Table 3: Dose limits for non-cancer effects. 19
Table 4: Test scenarios of TMP100 and TMP461. 59
Table 5: Bottom detection limit polynomials of both XChips. 69

List of symbols

Symbol	Unit	Description
V	[V]	Voltage
$V_{1\text{-}5}$	[V]	Voltage applied across parallel plates of gas-filled detectors

Abbreviations

Abbreviation	Meaning
ADC	Analogue-to-Digital Converter
ATLAS	A Toroidal LHC ApparatuS
CERN	the European Organization for Nuclear Research
COTS	Commercial Off The Shelf
CME	Coronal Mass Ejection
CMOS	Complementary Metal-Oxide-Semiconductor
DRAM	Dynamic Random Access Memory
EDA	Electronic Design Automation
ESA	the European Space Agency
GCR	Galactic Cosmic Rays
GEO	Geosynchronous Earth Orbit
GTO	Geo-Transfer Orbit
HEO	Highly Elliptical Orbit
I2C	Inter-Integrated Circuit
ICRP	International Commission on Radiological Protection
ID	IDentification
ISS	the International Space Station
LDEF	the Long Duration Exposure Facility
LEO	Low Earth Orbit
LET	Linear Energy Transfer
LVDS	Low-Voltage Differential Signaling
MEO	Medium Earth Orbit
MOS	Metal-Oxide-Semiconductor
NASA	the National Aeronautics and Space Administration
NIEL	Non-Ionizing Energy Loss
PCB	Printed Circuit Board
PVC	PolyVinyl Chloride

RAM	Random Access Memory
RDM	Radiation Design Margin
REID	Risk of Exposure-Induced Death
RTG	Radioisotope Thermoelectric Generator
SAA	the South Atlantic Anomaly
SEB	Single Event Burn-out
SEE	Single Event Effect
SEL	Single Event Latch-up
SEU	Single Event Upset
SF	Solar Flare
SOI	Silicon On Insulator
SOS	Silicon On Sapphire
SPE	Solar Proton Event
SPI	Serial Peripheral Interface
SRAM	Static Random Access Memory
TID	Total Ionizing Dose
UART	Universal Asynchronous Receiver-Transmitter
USB	Universal Serial Bus
UV	UltraViolet

1 Introduction

With the upcoming of space-related missions, the space environment and its effects on spacecraft and human crews are becoming more and more important. From tourist activities or space mining, all the way to colonizing planet Mars, more complex objectives lead to extensions of time spent above borders of our atmosphere resulting in significant load on both human crew and hardware components due to the space environment exposure. Among others, ionizing cosmic radiation has a major impact on the proper development of space missions as the result of its damaging properties. Moreover, cosmic radiation is highly variable. Missions beyond the Earth's magnetosphere suffer from being exposed without the protection provided by our planet. On the other hand, most missions orbiting the Earth are exposed to radiation belts that are not present beyond the Earth's magnetosphere. Accurate measurement of cosmic radiation, i.e. cosmic radiation dosimetry, provides an important insight not only in terms of hardware protection but also in terms of personal dose measurement for humans and becomes increasingly crucial in the future of space exploration.

2 Ionizing radiation

Radiation with enough energy to detach electrons from atoms and to produce ions, i.e. ionizing the atoms, is called ionizing radiation. Furthermore, ionizing radiation is categorized as either directly or indirectly ionizing based on the process of ionization. Direct ionization occurs as a result of interactions with charged particles with adequate kinetic energy to ionize atoms of the interacting material. Such particles include alpha particles, electrons, positrons and protons. Indirect ionization occurs as a result of interactions with high-energy photons and neutrons. These neutral particles produce secondary directly ionizing particles through interactions with the interacting material and cause ionization through secondary particles. Sources of ionizing radiation are being divided into naturally occurring or artificially generated man-made sources. Natural sources include radioactive isotopes and cosmic radiation. On the other hand, man-made sources involve ionizing radiation generators, such as X-ray tubes, nuclear reactors, particle accelerators and artificial radioactive isotopes. In general, five types of ionizing radiation are being distinguished, such as alpha particles, beta particles, gamma rays, X-rays, neutron radiation and charged nuclei. However, only the first three are described as they are the main forms of ionizing radiation. [1-2]

2.1 Alpha particles

Alpha particles are emitted as the result of alpha decay. The particle itself is a nucleus of helium, therefore alpha decay causes a decrease of atomic mass by 4 and a decrease of atomic number by 2. For instance, plutonium-239 or radium-226 emit alpha particles through radioactive nuclear decay. Since an alpha particle is missing two electrons, it carries two positive charges. Alpha particles produce positive and negative ions through interactions by removing electrons from atoms and are considered highly ionizing. However, their penetration radius is relatively small due to a rapid loss of energy during the ionization process. For example, the penetration depth of alpha particles is only a few centimetres of air or human skin. Nonetheless, more energetic alpha particles emerging from space are capable of penetrating human skin or even shielding of spacecraft when encountered in space. Energy resulted from alpha decay of various isotopic sequences of heavy nuclei is shown in Figure 1. [1-2]

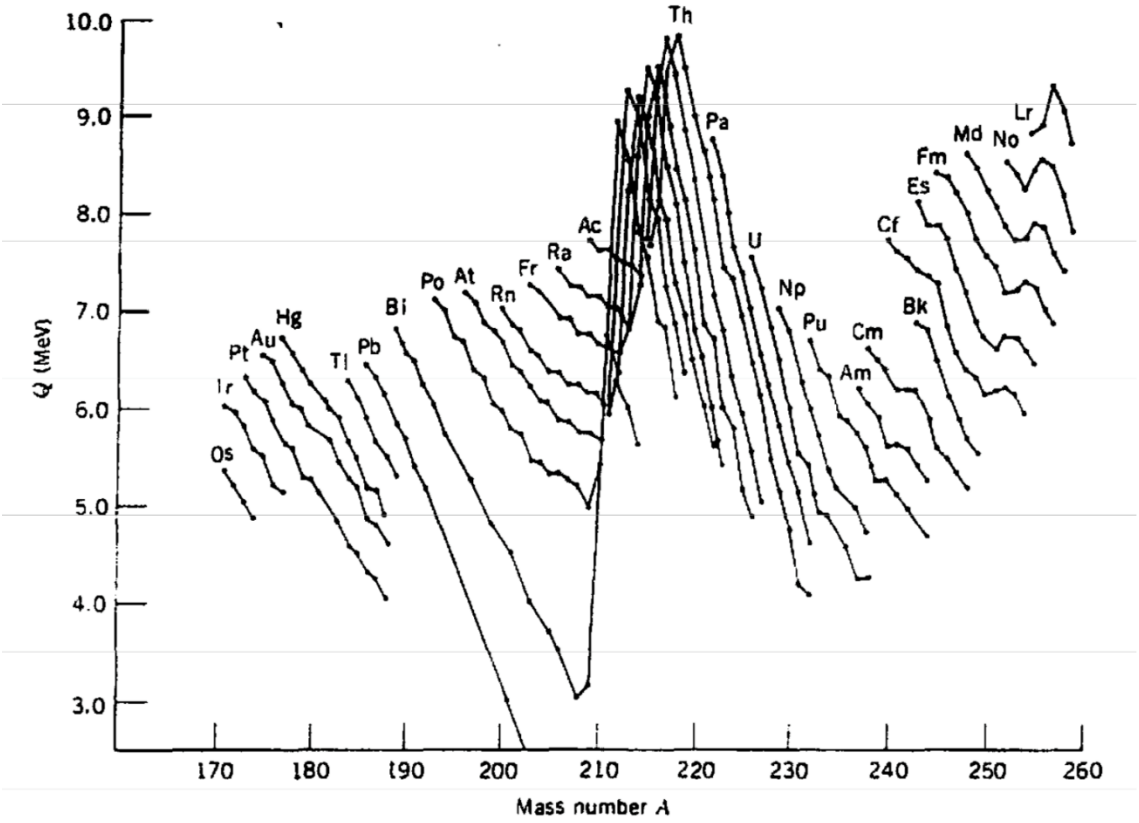

Figure 1: Measured energy resulted from alpha decay for various isotopic sequences of heavy nuclei. [1]

2.2 Beta particles

Beta particles are emitted as the result of beta decay in two forms. The two forms differ in nuclear processes leading to radiation of either electrons or positrons. In the case of electron beta decay, the electron radiation itself is preceded by the decay of a neutron into a proton, electron and antineutrino. Thus, electron beta decay causes an increase of atomic number by one and does not change atomic mass. Supposing positron beta decay, the positron radiation is preceded by the decay of a proton into a neutron, positron and neutrino. Hence, positron beta decay causes a decrease of atomic number by one and does not change atomic mass. This type of beta decay occurs mainly as an outcome of radioactive decay of artificial radioactive isotopes. In comparison with alpha particles, beta particles are of lower mass, smaller and less ionizing. Hence, their penetration radius is higher. For instance, the penetration depth of beta particles is a few metres of air or a few millimetres of aluminium. Commonly used sources of electron beta radiation are sulfur-35 or chlorine-36. Energy distribution of chlorine-36 is shown in Figure 2. [1-2]

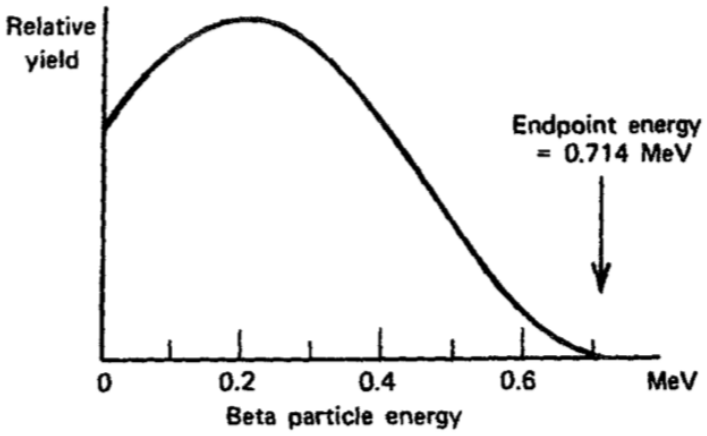

Figure 2: Energy distribution of chlorine-36. [1]

2.3 Interactions of beta particles

Three different events, such as ionization, elastic scattering and bremsstrahlung, may occur as a result of beta particles interactions with a material. Ionization is the main part of the energy loss of beta particles. Elastic scattering is caused by the influence of electric forces in a nucleus and by electrons bounded to the nucleus. This event changes the direction of beta particles. Mainly slow, low-energy particles suffer from elastic scattering. Bremsstrahlung, i.e. braking radiation, is a consequence of the deceleration of beta particles while flying through electric fields of atoms. This event produces radiation far more powerful and penetrating than beta particles called X-rays. The percentage of generated braking radiation and its energy not only relates to the energy of beta particles but also to the atomic number of the absorbing material. This fact needs to be considered when designing a shielding material. Materials consisting of light elements are preferred. Moreover, in the case of a positron's interaction with a material, an event called annihilation occurs. Annihilation is caused by a collision of an electron and a positron and leads to radiation of two gamma rays of specific energy equal to 511 keV. Therefore, every positron source is also a source of gamma rays. [1-2]

2.4 Gamma rays

Gamma rays normally occur following alpha or beta decay. Since an atom resulting from alpha or beta decay is left in an excited state, it decays into a lower energy state by emitting a gamma ray in a process called gamma decay. Atomic number and atomic mass do not change during this process. In general, a gamma ray is electromagnetic radiation with a very short wavelength in the order of 10^{-11} to 10^{-13} m. For example, commonly used gamma-ray sources are cobalt-60 or caesium-137. The energy emission spectrum of each radionuclide is specific and given by the characteristic of the radionuclide's decay. A measured gamma-ray spectrum resulted from gamma decay of metastable hafnium-180 is illustrated in Figure 3. The penetration radius of gamma rays is higher than of beta particles due to the lack of charge and of Coulomb interactions. The material used for shielding gamma rays is usually being categorized by the thickness required to reduce the intensity by 50 %. Very dense materials with high atomic number such as lead are the best choices for shielding gamma rays. [1-2]

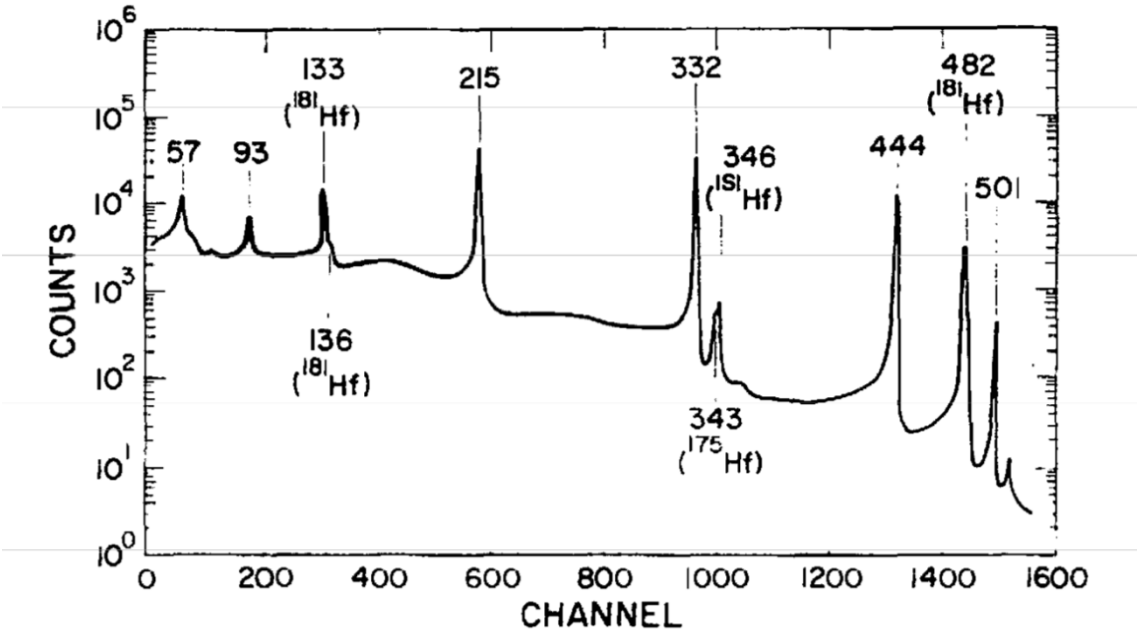

Figure 3: The measured gamma-ray spectrum resulted from gamma decay of metastable hafnium-180. The spectrum contains also other isotopes of hafnium produced within the experiment. Gamma rays from each isotope are labelled. [1]

2.5 Interactions of gamma rays

Interactions of gamma rays with a material significantly differs from interactions by beta particles. Gamma rays are indirectly ionizing. While passing through a material, gamma rays release energy by three different processes, such as the photoelectric effect, Compton scattering and pair production. [1-2]

The photoelectric effect occurs when photons with enough energy transfer their energy to atom's electrons. Consequently, an irradiated electron, i.e. a photoelectron, is ejected and replaced by a new one. During this transition, redundant energy is emitted in the form of a photon. This photon usually lacks enough energy to produce another photoelectric effect and is absorbed by the surrounding material. Hence, the photoelectric effect is in most cases considered an absolute absorption of gamma rays. The probability of the photoelectric effect increases with atomic number of the material and decreases with increasing energy of gamma rays. Common energy of gamma rays causing the photoelectric effect are of the order of a few keV. [1-2]

Compton scattering is an interaction of a photon with a charged particle and in most cases with a free or poorly bonded electron. A gamma ray or X-ray transfers part of its energy to an electron, shifts it and changes its own direction of flight. Compton scattering is considered a mid-energy phenomenon since the energy required for Compton scattering is higher than for the photoelectric effect but not as high as required for pair production. Furthermore, Compton scattering occurs mainly as an interaction with a material with low atomic number. [1-2]

Pair production is the result of a material interaction with gamma rays with energy higher than approx. 1 MeV. This energy corresponds to the rest mass energy of electrons and positrons. In general, an electron-positron pair is a product of an absorption of a gamma ray passing in the proximity of an atomic nucleus. The possible redundant energy of the absorbed gamma ray is converted into the kinetic energy of the pair. Additionally, the resultant positron is quickly transformed into two gamma rays of energy equal to 511 keV due to the annihilation process caused by the collision with an electron. Dominant regions for each gamma-ray interaction are shown in Figure 4. [1-2]

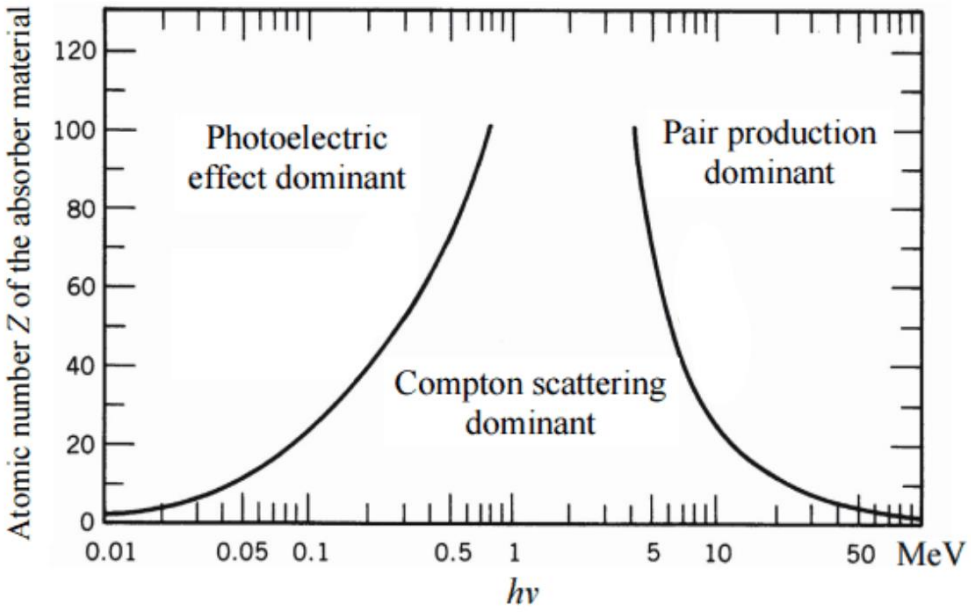

Figure 4: A demonstration of three separate regions of dominant interactions. The regions are divided based on the initial energy of a gamma ray and atomic number of the absorbing material. [3]

3 Ionizing radiation in space

Ionizing radiation originated in space is called cosmic radiation. Three main types of cosmic radiation are being distinguished based on their source. These are:

a) Galactic Cosmic Rays (GCR),
b) The solar wind and Solar Particle Events (SPE),
c) Trapped radiation. [4]

3.1 Galactic cosmic rays

GCR is an interstellar mass accelerated by explosions of supernovae that originates in galactic or extragalactic space. It consists primarily of protons (~88 %) and ionized heavy nuclei, mainly nuclei of helium (~11 %). The remaining 1 % consists of all heavy elements. However, ions heavier than Ni are not usually taken into consideration due to their low abundances. Elemental abundances are shown in Figure 5. The energy of GCR is usually ranging from 1 MeV to as much as 10 GeV but can rarely reach up to extreme energy such as 10^{20} eV. Nevertheless, the GCR energy spectrum within our solar system is peaked around 1 GeV. The maximum flux of particles at this energy is approx. $3 \cdot 10^{11}$ particles per m^2 per year. The flux of more energetic particles decreases with the third power of the energy. For example, the flux of GCR with the energy of 10^{10} MeV is approx. 3 particles per m^2 per year. Moreover, because of the changing volume of plasma in the solar wind throughout the 11-year-long solar cycle resulting in changes in interplanetary magnetic fields, the Sun affects GCR intensities during its cycle. For that reason, the intensity of GCR is highest when the Sun is at its minimum level of activity and vice versa. [4-7]

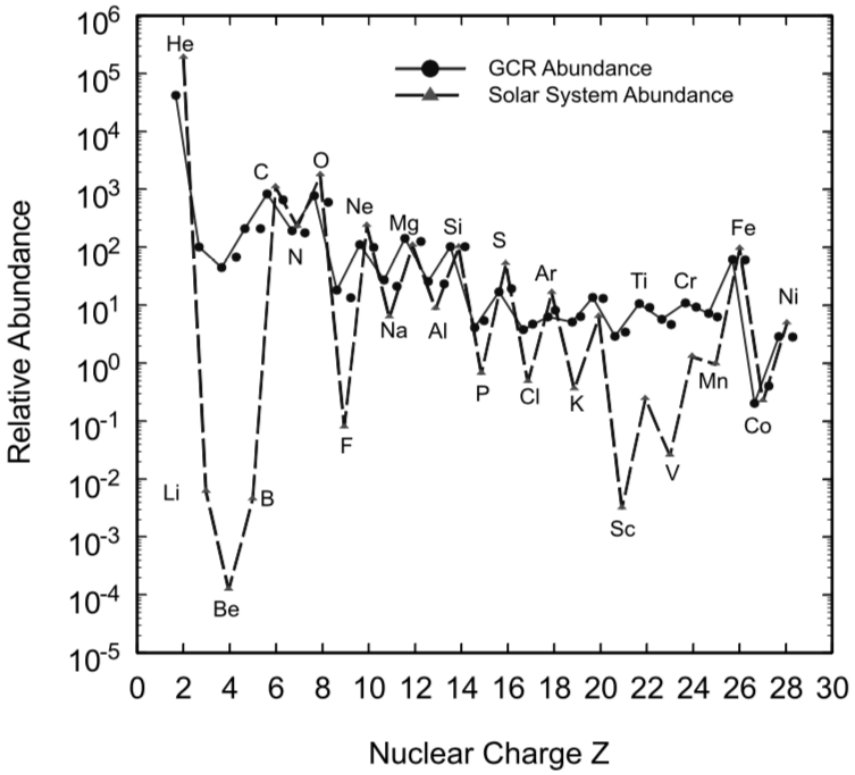

Figure 5: Elemental abundances of GCR for ions from He to Ni together with solar system abundances for the same elements. Elements with nuclear charge greater than Ni are not illustrated due to their low abundances. [6]

3.2 The solar wind and solar particle events

Radiation load caused by the Sun is of two kinds. At first, there is the continually emitted solar wind with energy up to 10 keV which consists primarily of electrons and protons moving radially away from the Sun and posing relatively low radiation hazard for spacecraft. In contrast with the continuous solar wind, SPE occur randomly during the solar cycle and cannot be exactly predicted. It is only known that they appear more often in the phase of the solar activity maximum and the most intense events are observed at the end of this phase. Typical solar events generating SPE are Coronal Mass Ejection (CME) and Solar Flares (SF) usually lasting for days, respectively hours. SPE consist mainly of protons, nuclei of helium, but also high-nuclear-charge particles are present with abundances varying significantly between individual events. The energy of these particles generally does not exceed 100 MeV but can rarely reach a few GeV. Comparison of sunspot numbers and solar proton fluences is shown in Figure 6. [4-7]

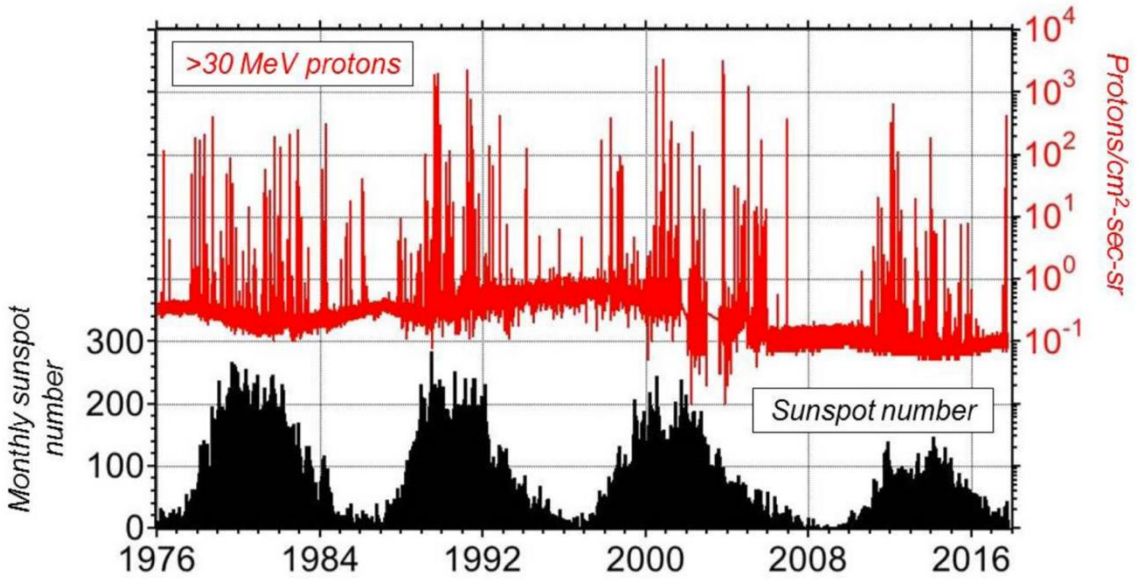

Figure 6: Comparison of solar proton fluences with energy higher than 30 MeV and the sunspot quantity representing the solar cycle of the Sun. [4]

3.3 Trapped radiation - Van Allen belts

At certain altitude over the Earth's surface are mostly protons, electrons and a small percentage of heavy ions, such as O^+, trapped by the Earth's magnetic field in a formation of a toroidal belt. This toroid is usually being divided into two zones called the inner (low-altitude) and the outer (high-altitude) Van Allen belt. [4, 5, 9]

The inner belt spreads from an altitude of hundreds of kilometres to several thousands of kilometres and consists mainly of protons and electrons with energy of tens of MeV and hundreds of keV, respectively. Because of the relatively strong magnetic field in the region of the inner belt, the inner belt zone is stable. Nevertheless, changes may occur with an increase in the solar activity. Furthermore, because of the shifted centre of the Earth's magnetic field to the Earth's centre by approx. 500 km towards the Western Pacific and the inclined dipole at about 11.5 ° with respect to the Earth's rotation axis, the inner belt drops in the South Atlantic as far as to almost 400 km of altitude causing the so-called South Atlantic Anomaly (SAA). In fact, this phenomenon causes the most intense radiation in Low Earth Orbit (LEO) and significantly endangers satellites orbiting at several hundred kilometres of altitude, for example, the International Space Station (ISS). The significance of the SAA is demonstrated in Figure 7. [4, 5, 9]

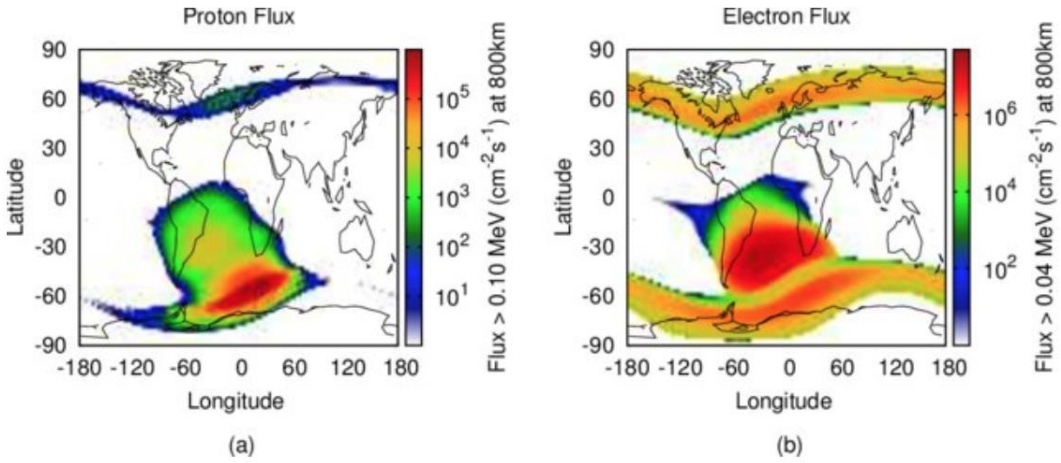

Figure 7: The proton and electron flux over the South Atlantic reconstructed based on AP8MAX, resp. AE8MAX models and representing conditions for the solar activity maximum. [10]

The outer belt is populated by electrons of energy up to 10 MeV and stretches up to 60 000 km of altitude. Therefore, the outer belt is more influenced by the variability of the Earth's geomagnetic tail and undergoes greater temporal changes, such as the change of electron concentrations as much as 1000 times. Both Van Allen belts are shown in Figure 8 along with the illustration of proton and electron densities. [4, 5, 9]

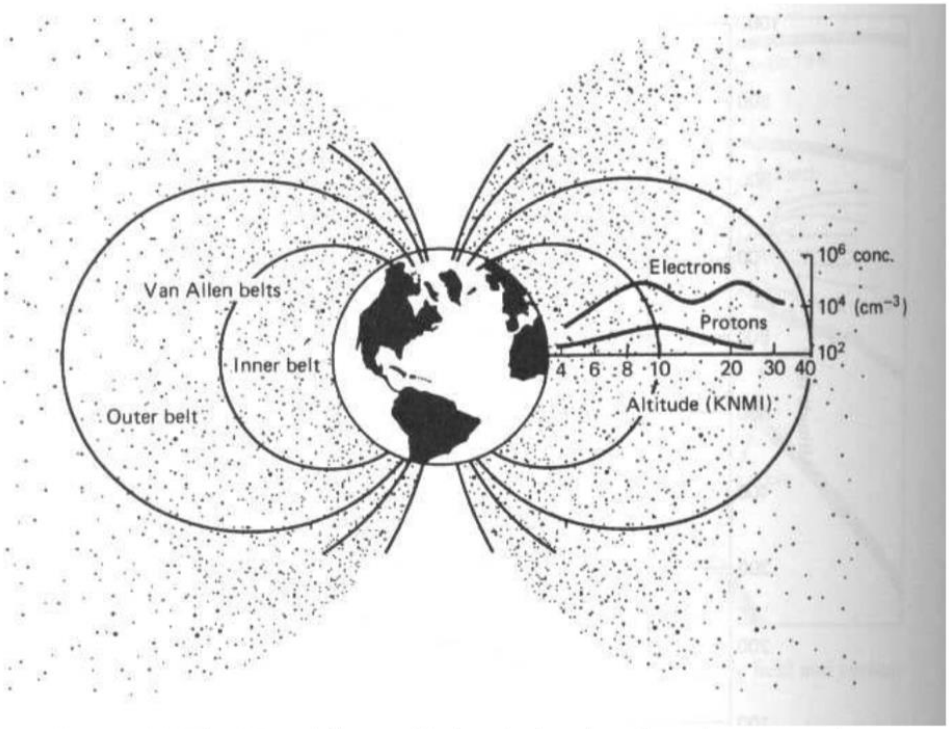

Figure 8: The Van Allen radiation belts showing proton and electron densities. [11]

4 Effects of ionizing radiation on electronic hardware components

Exposing hardware components to radiation sources discussed above leads to temporary or permanent disruptions in their proper operation due to an energy deposition of energetic particles inside microelectronics circuits. This energy deposition is measured in the rad, i.e. radiation absorbed dose, or the gray units (1 Gy = 1 J/kg = 100 rad) and is expressed for a specific material being considered. Two basic mechanisms of energy depositions in semiconductor materials are being distinguished:

a) production of electron-hole pairs (ionization),
b) atomic displacement,

causing different types of corruptions in microelectronics. [11, 12, 13]

4.1 Total ionizing dose effects

An interaction of high-energy protons and electrons with a spacecraft's body material produces deeply penetrating ionizing radiation and causes Total Ionizing Dose effects (TID). TID effects express the cumulative absorption of ionizing radiation of a spacecraft material over long time periods leading to changes in parameters of electronics and eventually to a failure. As a consequence of this, TID usually determines the operational lifetime of spacecraft electronics. The penetration depth and the intensity of radiation depends on the type of the shielding material and its thickness as shown in Figure 9. Commonly used aluminium shields can effectively reduce the radiation dose caused by electrons and low-energy protons. Protons with energy higher than 30 MeV are difficult to be shielded. [11-14]

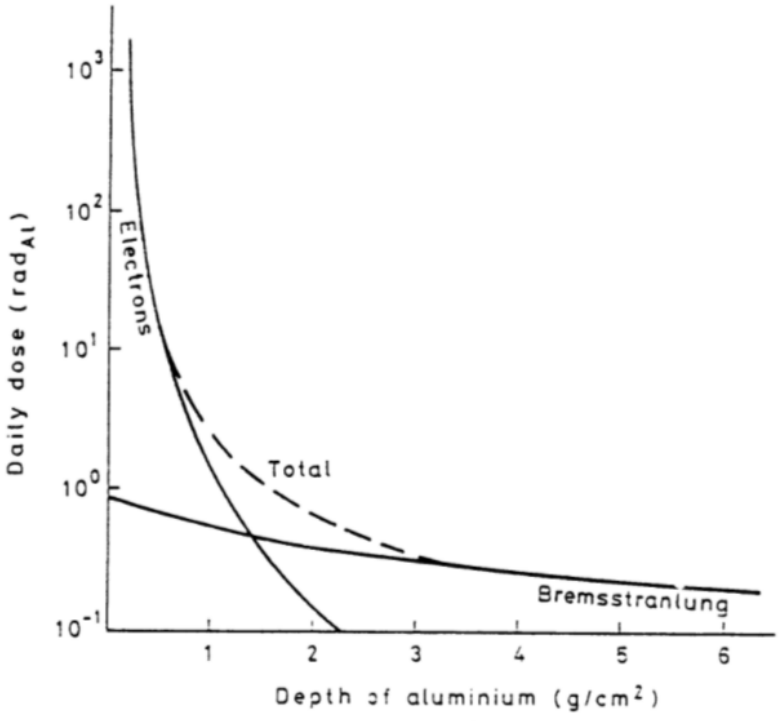

Figure 9: The dependency of the radiation intensity on the thickness of a shielding material. [13]

A value of approx. 1000 rad of ionizing radiation is enough for sensitive silicon microcircuits to cause a failure. For comparison, hardened silicon electronics can withstand as much as 1000 times more. [11-14]

4.2 Single event effects

When a charged particle, such as an electron, proton or heavy ion, collides with a semiconductor, it loses its energy by nuclear interactions and causes a condition referred to as Single Event Effect (SEE). The interactions appear as an ionized track of electron-hole pairs in the direction determined by the particle's trajectory and the magnitude dependent on the particle's type and the energy. This phenomenon is also referred to as Linear Energy Transfer (LET). Furthermore, SEE is being classified into three categories:

a) Single Event Upset (SEU),
b) Single Event Latch-up (SEL),
c) Single Event Burn-out (SEB). [11, 12, 13, 15]

SEU results in changing the logic state of a digital microelectronic device. This anomaly is temporary since the device can be restored to its original state and is referred to as a soft error. The occurrence of SEU measured while orbiting the Earth at an altitude of 800 km is demonstrated in Figure 10. It is noticeable that the majority of events occurs in the SAA region, while other events appear mostly at high latitudes both as the result of Van Allen radiation belts presence. A related phenomenon to SEU is SEL, an anomaly which is permanent due to the abnormally high-current state resulting from passages of charged particles through a sensitive region. This type of SEE damages the device in a way that it cannot be restored to its original state. Consequently, when the device has no current limitation, SEL can cause abnormally large currents passing through its circuits and damaging the device even more, i.e. causing SEB. [11, 12, 13, 15]

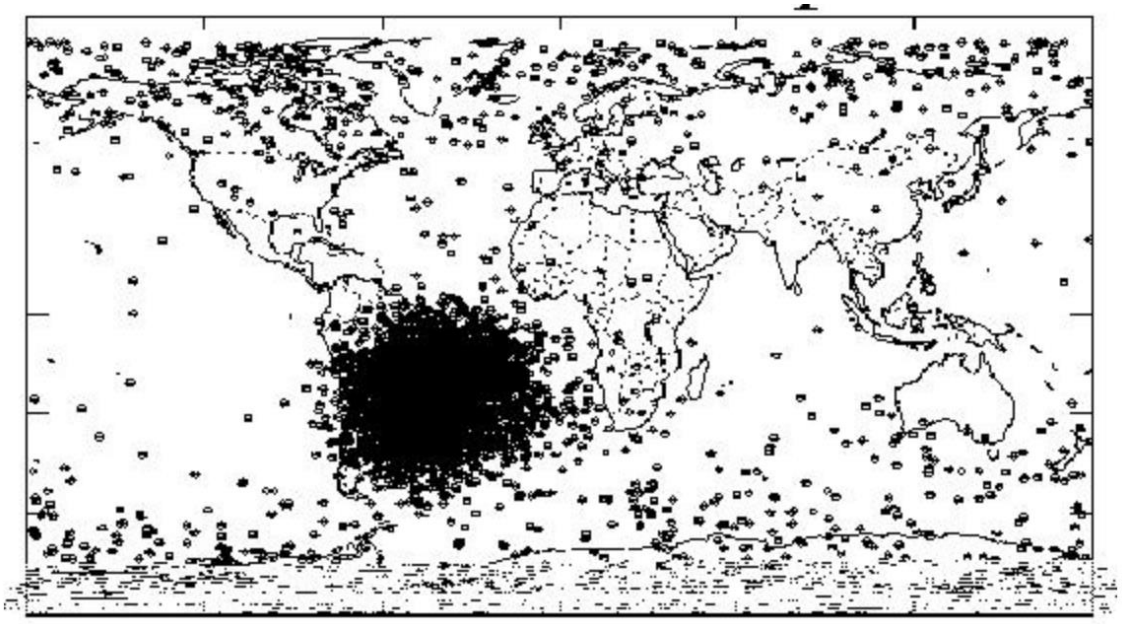

Figure 10: SEU recorded by the UOSAT-3 spacecraft orbiting at an altitude of 800 km (axis x and y are representing longitude and latitude, respectively). [16]

4.3 Displacement damage effects

All effects described above are caused by the production of electron-hole pairs, i.e. ionization. However, if an atom is displaced from its usual lattice site, takes an interstitial position instead and leaves a vacancy behind, the second mechanism of the energy deposition in semiconductor materials develops, i.e. displacement damage effect. This effect is mainly caused by protons but also high-energy electrons with energy over 180 keV and other heavy particles. Subsequently, regions where multiple displacement damage effects cumulate are addressed as defect clusters.

As a consequence of defect clusters, device's properties and its performance are being altered. For example, by increasing the resistance of solar cells, displacement damage effects continuously degrade solar panels and reduce the generated power. Radiation-induced degradation of multiple types of solar cells is shown in Figure 11. [11, 12, 13, 17]

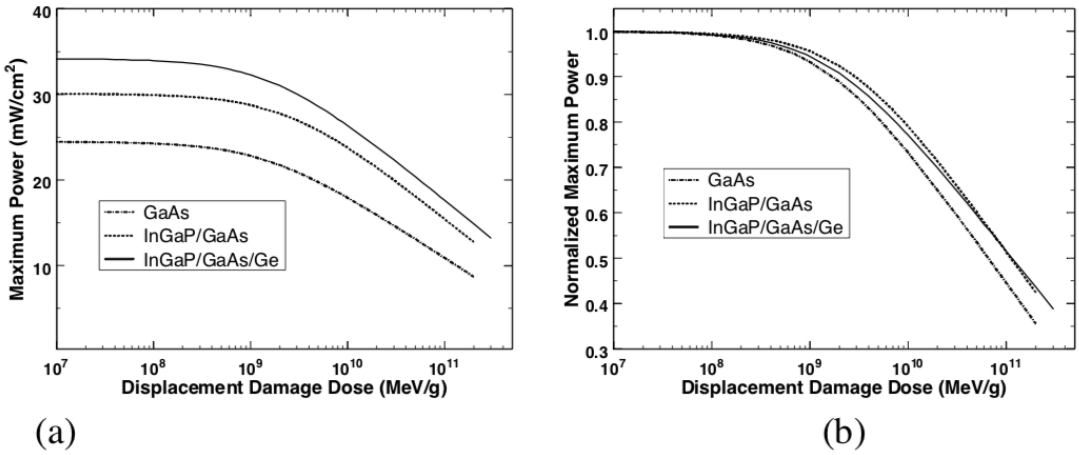

Figure 11: Radiation-induced degradation of single-junction, dual-junction and triple-junction solar cells depicted on absolute (a) and normalized (b) scale. [18]

5 Effects of ionizing radiation on humans

Ionizing radiation is considered to be one of the biggest threats to humans in any space-related mission and it has developed into a very serious problem especially for Mars or other beyond the Moon explorative missions due to their long duration. With present technology options, shielding materials are not capable to fully absorb cosmic radiation. Hence, even protected by spacecraft, its crew inevitably suffers from the cosmic radiation exposure. The radiation environment at the surface of an astronaut's body is a result of interactions of all types of cosmic radiation described above with the material of spacecraft or a spacesuit except for interplanetary missions where ionizing radiation from Van Allen belts is not present. For example, GCR has a penetration radius of several tens of centimetres considering an aluminium material. Consequently, the nuclear interactions between GCR particles, shielding material's nuclei and spacecraft's structure in general produce particles of lower atomic numbers with lower LET leading to a greater range of penetration than the primary particles. The radiation environment at the surface of a spacesuit worn on the Moon is demonstrated in Figure 12. [19, 21, 22, 23]

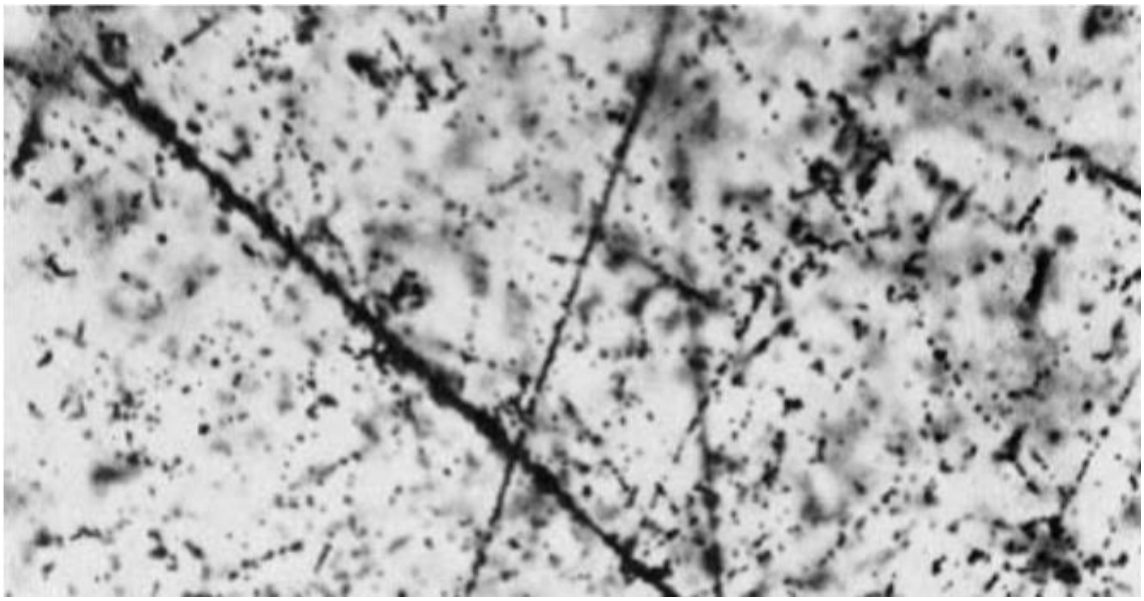

Figure 12: A microscopic view of an Ilford G.5 nuclear emulsion that was worn by Neil Armstrong on his ankle during the Apollo 11 mission on the Moon showing numerous proton paths and one track of a heavy ion with estimated atomic number of 12. [19]

Along with the gray (Gy) unit mentioned earlier, another unit related to ionizing radiation is often used, i.e. the sievert (Sv). Unlike the gray being a representation of an actual physical dose, the sievert is used as an equivalent and an effective dose and recognizes types of radiation and specific sensitivities of irradiated tissues, respectively. For example, alpha radiation is approx. 20 times more dangerous than gamma radiation. Therefore, 1 Gy of gamma radiation corresponds to 1 Sv of an equivalent dose, but 1 Gy of alpha radiation corresponds to 20 Sv of an equivalent dose. Moreover, the unit allowing calculation of the cumulative effect of doses caused by different radiation has no generally established name and is usually referred to as the gray-equivalent, Gy/Eq or Gy-Eq. [20]

The effect of ionizing radiation on the human body can be categorized as either acute or delayed. With the exception of very large solar eruptions, delayed effects resulting in carcinogenesis are the main concern. Based on an average cell's area, statistical data regarding cosmic radiation fluences and anatomical models, it is possible to estimate exposure levels for a various type of missions. For instance, the example of NASA's estimated exposure levels for a set of reference missions with the shielding of 10 g/cm^2 and ICRP 60 quality factors along with NASA's historic missions are shown in Table 1. However, the exposure levels are constantly being updated and revised. [19, 22]

Table 1: Exposure levels for an example of reference missions estimated by NASA and historic missions for comparison [19, 22].

Mission	Duration of mission	Dose
Space shuttle mission	8 days	6 mSv
Apollo 14	9 days	11 mSv
the ISS mission	6 months	160 mSv
Deep-space mission	1 year	385 mGy-Eq
Mars mission with the solar minimum	3 years	1000-1200 mSv

NASA also declares that an astronaut's exposure to radiation must not lead to more than 3 % risk of a radiation-induced death from fatal cancer (3 % REID) in terms of an effective dose received throughout an astronaut's career. However, because of the carcinogenesis being a complex and not fully understood problem and exposure levels being an estimate, the risk projection calculation is a matter of uncertainty. Furthermore, the risk depends on age and gender as a result of latency effects, tissue and average lifespan differences. Table 2 summarizes career effective doses for a 1-year mission for a 3 % REID. [21]

Table 2: Effective dose limits for a 1-year mission, 3 % REID according to NASA [21].

	Effective dose (mSv)	
Age at exposure	Male	Female
30	620	470
35	720	550
40	800	620
45	950	750
50	1150	920
55	1470	1120

Effective dose limits grow with increasing of astronaut's age since it is assumed that an exposure to more radiation in early age might lead to greater health risks during old age. [22]

Not only the carcinogenesis but also non-cancer effects are being considered. Such effects might include tissue degeneration caused by collective cell destruction leading to a cardiovascular disease, central nervous system degenerative disorders or acute radiation syndromes. Dose limits for non-cancer effects for different types of tissue, mission durations and total career limits is shown in Table 3. Values are given in mGy-Eq units since the radiation exposure might originate from more types of cosmic radiation. For comparison, exposure limits for the general public are approx. 100 times lower. [19]

Table 3: Dose limits for non-cancer effects for different mission durations and career limits for various types of tissue defined by NASA. [21]

Type of tissue	30-day limit (mGy-Eq)	1-year limit (mGy-Eq)	Career limit (mGy-Eq)
Lens	1000	2000	4000
Skin	1500	3000	6000
Blood-forming organs	250	500	-
Heart	250	500	1000
Central nervous system	500	1000	1500

Based on cosmic radiation, its damaging effects on spacecraft and its crew described in the previous chapters, it is important to measure the amount of radiation received, i.e. the radiation exposure, since the consequences from the exposure limits excess can be in many cases fatal for the mission or can result in loss of life. [24, 25]

6 Ionizing radiation detection techniques

Because every type of cosmic radiation described in the previous chapters contributes to the radiation exposure, the actual radiation flux, charge and energy of particles vary significantly. Variables include the altitude, inclination and spacecraft's orientation relative to the Sun and the Earth. Moreover, the phase of the solar cycle is crucial due to the increased frequency of CME and SF in the solar maximum and vice versa. Also, additional variabilities are brought by the mission's nature as missions beyond the Earth's magnetosphere would not experience the presence of Van Allen belts. On the other hand, missions in interplanetary space suffer more from the increased flux of GCR, solar wind and SPE due to the lack of protection from the magnetic field of the Earth. All in all, the radiation environment in space consists of particles of various kinds with a wide range of energy and flux as shown in Figure 13. Additionally, demands on dosimetry instruments operating in space are far more increased in comparison with the ground-based. Besides accuracy and wide dynamic range, space-based dosimetry instruments should be relatively small, with low power consumption and of low mass to reduce launching costs and durable in order to withstand the constant use since space missions lack spare or redundant parts. For these reasons, accurate radiation dosimetry in space is considered to be a demanding but necessary challenge. [24, 25]

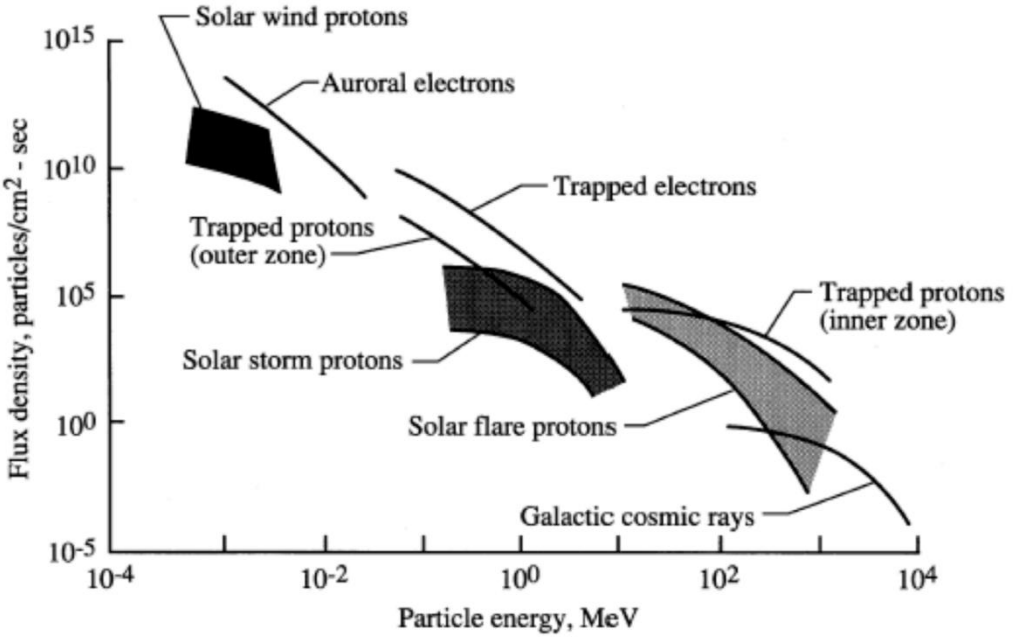

Figure 13: The energy and flux of cosmic radiation. [21]

As the main concern of this thesis is environmental testing of the SpacePix detector, i.e. a pixel semiconductor detector, the main focus of this chapter regarding ionizing radiation techniques will be on semiconductor detectors, although other historical and current techniques are also covered.

6.1 Gas-filled detectors

Gas-filled detectors exploit the characteristic attribute of ionizing radiation, i.e. the ability to detach electrons from atoms or molecules while passing through a material. Therefore, radiation can be measured by a simple sum of ion-electron pairs produced by the radiation in the radiation-absorbing material. Such a detector consists of a parallel plate capacitor filled with gas. Since ions travel to the negative cathode plate and electrons travel to the positive anode plate, parallel plates prevent recombination of the pairs and provide an option to measure ionizing radiation as the generated electric signal. [26-30]

Three types of gas-filled detectors are:

a) Ionization chambers,
b) Proportional counters,
c) Geiger-Müller counters. [26-30]

Gas-filled detectors can be distinguished by the applied voltage leading to differences in the ion-electron pair collection and limitations as shown in Figure 14.

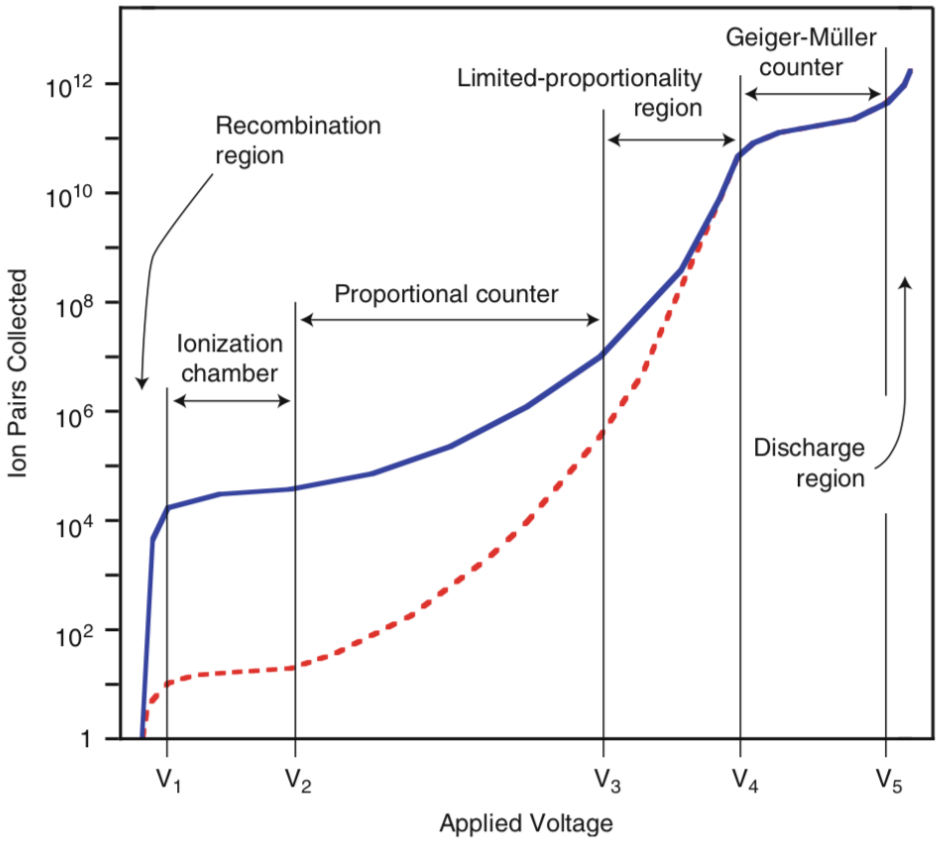

Figure 14: The dependency of the number of ion-electron pairs on the applied voltage along with gas-filled detectors operation ranges. The two curves illustrate radiation that deposit different energy and cannot be distinguished in certain regions. [29]

6.1.1 Ionization chambers

After a certain threshold (V_1 as shown in Figure 14), the electric field applied across parallel plates is strong enough to prevent ion-electron pairs from recombination but not strong enough to produce any secondary ion-electron pairs. Detectors operating in the region where $V_1 < V < V_2$ are classified as ionization chambers since these detectors only collect the charge generated directly by the incident radiation, i.e. the primary ion pair production. A dry air gap is usually used as a dielectric. The average energy required to produce an ion-electron pair in dry air is approx. 30 eV. Considering two square parallel plates with 10 cm each side separated by a 1 cm gap of dry air and a 2 MeV gamma-ray source, the resulting voltage pulse would be approx. 1 mV. Therefore, the radiation detection requires amplification of the detected voltage. Furthermore, pulse-type and current-type ionization chambers are being distinguished and designed either to generate voltage pulses by a rapid collection of electrons or to collect electrons continuously to

measure the amplified direct current, respectively. Schematic illustration of ionization chamber is in Figure 15. [26-30]

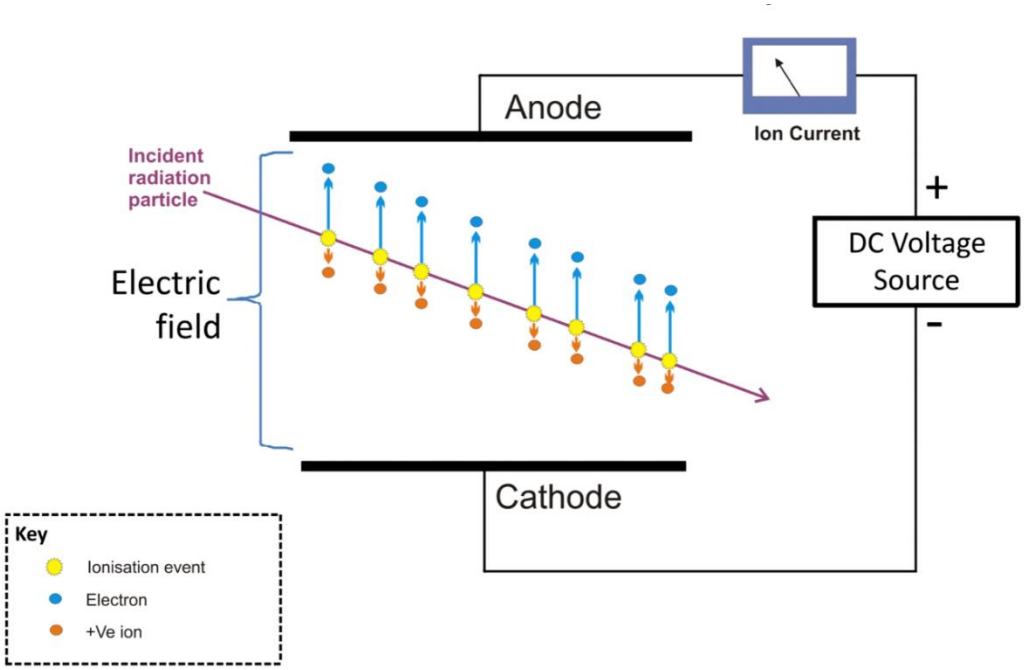

Figure 15: Schematic illustration of ionization chamber. The incident radiation particle interacts with gas molecules to produce ion-electron pairs. [27]

6.1.2 Proportional counters

The applied voltage exceeding the threshold V_2 from Figure 14 leads to the acceleration of ions and electrons. Electrons with enough energy are capable of additional ionization of other gas molecules resulting in the production of more free secondary electrons, i.e. the gas multiplication. Since the secondary electrons are accelerated too, this process leads to a so-called Townsend avalanche. Because of this avalanche, each original ion-electron pair in this process induces approx. other 10^4 events. The incident particle energy can be measured as the result of the proportional relationship between secondary events and primary events. In other words, the output signal is proportional to the energy deposited in the chamber. Therefore, detectors operating in the region where $V_2 < V < V_3$ are called proportional counters. A mixture of 90 % argon + 10 % methane is generally used as a dielectric. Schematic illustration of proportional counter is in Figure 16. [26-30]

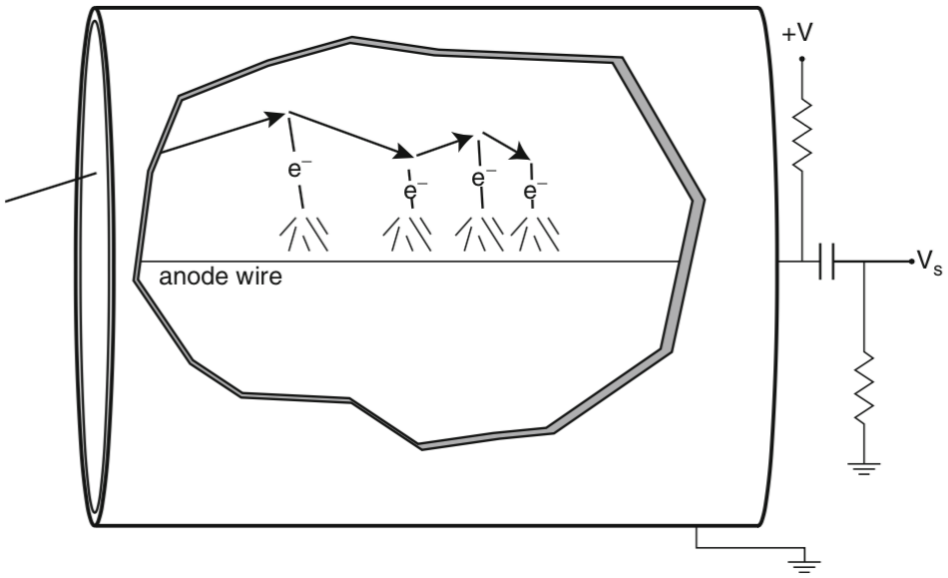

Figure 16: Schematic illustration of proportional counter. The accelerated electron from original ion-electron pair interacts with gas molecules to induce multiple avalanches. [29]

6.1.3 Geiger-Müller counters

Increasing the applied voltage beyond the threshold V_3 as shown in Figure 14 introduces more total ionization through the gas multiplication but reduces the proportionality as the result of ion cloud generation in the proximity of the anode. Hence, the region where $V_3 < V < V_4$ is referred to as the limited-proportionality region. Geiger-Müller counters operate in the region where $V_4 < V < V_5$, i.e. the Geiger plateau. As demonstrated in Figure 14, distinctive energy deposited by different radiation are not distinguishable. Furthermore, collected ion pairs do not change significantly with changes in the applied voltage as illustrated in Figure 17. This is caused by a large potential in the active region of the detector leading to multiple avalanches. When a great number of slow-moving ions form in the proximity of the anode, a so-called space charge reducing the magnitude of the electric field occurs. Consequently, the attractive force accelerating secondary electrons diminishes and all radiation interacting with the detector generates the same current. Inert gases are usually used as a dielectric. [26-30]

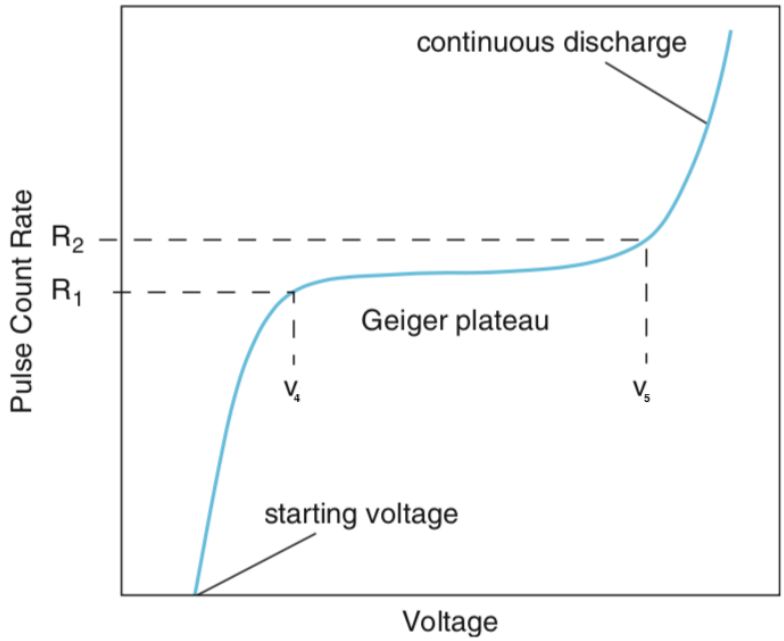

Figure 17: The Geiger plateau curve. The pulse count rate changes only slightly with the change of the applied voltage.

Finally, beyond the V_5 threshold occurs the region of continuous discharge since a further increase in voltage beyond the threshold V_5 causes a continuous breakdown in the gas. The resulting steady current flow emerges regardless of the radiation presence and can cause a damage to the detector. For this reason, Geiger-Müller counters are generally operated at the voltage in the middle of the Geiger plateau. [26-30]

Gas-filled detectors are generally easy to operate but lack the radiation detection efficiency. The low density of air or inert gas is sufficient for electrons, ions, low-energy X-rays and gamma rays. On the other hand, e.g. high-energy photons need a material of higher density to be stopped effectively. For example, given the density of air, standard temperature and pressure, a 78-meter-thick detector would be needed to attenuate a 1 MeV photon by half. [26-30]

6.2 Scintillation detectors

The detection principle of scintillation detectors varies from gas-filled detectors significantly since more steps of the detection are involved. At first, incident radiation ionizes an atom of a scintillation material resulting in fluorescence, i.e. emitting a photon of light. Afterwards, this photon hits a surface of a photomultiplier called the photocathode. The purpose of

a photomultiplier is to convert a photon into a photoelectron through the photoelectric effect and sufficiently multiply it in order to produce a measurable signal. After hitting the photocathode, the photoelectron is accelerated through a potential across individual dynodes and multiplied as the result of secondary emissions of electrons as shown in Figure 18. [26-30]

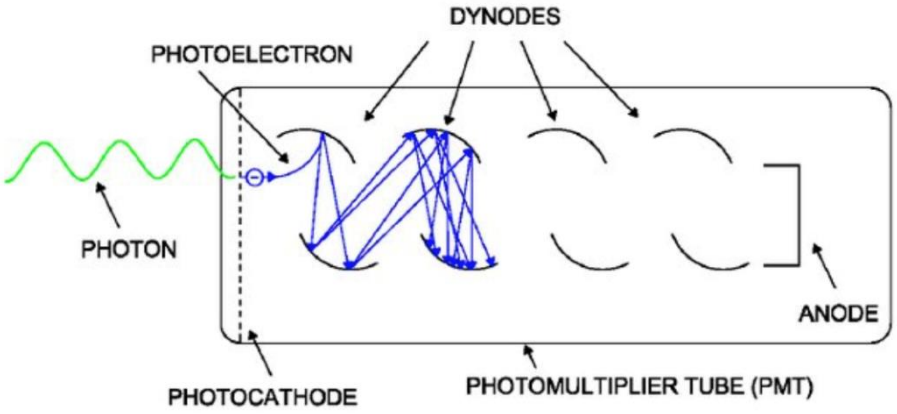

Figure 18: Schematic illustration of a photomultiplier tube demonstrating the photoelectron production and secondary emissions of electrons on individual dynodes. [32]

Organic and inorganic crystals, organic liquid, plastic and glass or gas can be used as a scintillation material with various properties, such as the decay time constant, index of refraction or formability, depending on the detection application. For instance, commonly used scintillator materials are organic crystals anthracene and stilbene or the plastic general-purpose scintillator NE-102A. [26-30]

The main advantage of scintillation detectors over gas-filled detectors is their solid active area resulting in better efficiency for high-energy radiation. Therefore, scintillation detectors are widely applied for high-energy photons or gamma-ray detection, in nuclear medicine in thyroid probes, well counters, gamma cameras or positron emission tomography. Another advantage over gas-filled detectors is the ability to determine the energy of received radiation, therefore identify radionuclides based on their energy. [26-30]

6.3 Semiconductor detectors

Since the principle of detection highly resembles gas-filled detectors, semiconductor detectors are commonly referred to as solid-state ionization chambers. Similarly, the active part of the detector is ionized as the result of an interaction with incident ionizing radiation and generates a pulse of voltage. Unlike gas-filled detectors, the solid-state sensing part of semiconductor detectors is denser than gas and stops the incident radiation more efficiently per unit length. Insulators and conductors are not used due to the insulating capability leading to the inhibition of charge collection and the rapid recombination of ion-electron pairs, respectively. Hence, only semiconductor materials are being used for solid-state ionization detectors, such as germanium and silicon. Early semiconductor detectors were constructed from extremely pure materials since they exploited ionization of undoped semiconductors and were difficult to manufacture. Modern detectors rely on semiconductor junction diodes and the property of their rectifying junction to allow a flow of current only in one direction. Incident radiation causes a pulse of current flowing in the opposite direction to the regular current flow through a diode and creates a directly measurable outcome. A detailed principle of the operation is described in the following paragraphs. [26-31]

The crystal lattice structure of silicone is shown in Figure 19. Each silicon atom is bounded by four electron pairs to the adjoining atom. Since the electrons are not free to drift in this crystal structure, undoped silicon is a weak conductor. Figure 19 along with the silicon lattice structure contains silicon's energy levels. Above the valence band formed by silicon's valence electrons is a region referred to as the forbidden or the band gap. The valence band represents a level with electrons tightly held in their orbit. The forbidden gap is approx. 1 eV of energy for undoped silicon. Above the forbidden gap is the conduction band where electrons have enough energy to drift freely throughout the crystal and conduct electricity. [26-31]

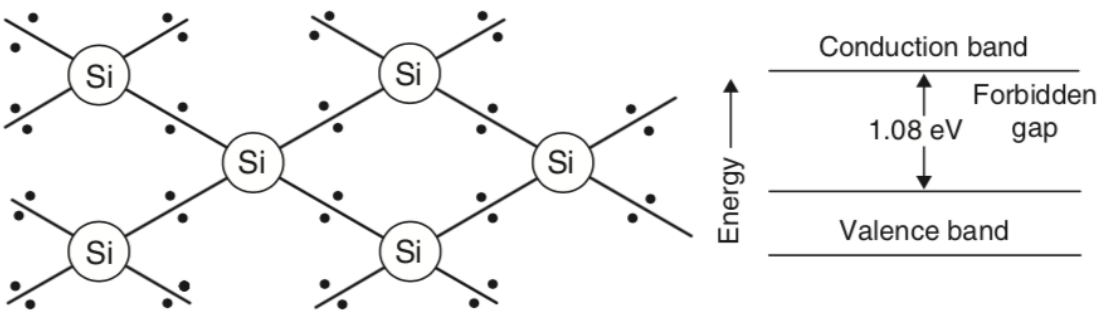

Figure 19: The crystal lattice structure of silicon along with undoped silicon's energy levels. [30]

Furthermore, when is a silicon atom in the crystal lattice structure replaced with phosphorus, a situation demonstrated in Figure 20 arises. Since phosphorus has five valence electrons, four will be used to form electron pairs in order to bond to adjoining silicon atoms and the fifth will be easily removed and free to drift throughout the crystal lattice to conduct electricity. As shown in Figure 20, a new energy level, i.e. the donor band, with a small step to the conduction band of approx. 0.05 eV is introduced and occupied by the fifth electron. A transfer of the fifth electron into the conduction band is relatively easy. Since the charge carried through the crystal structure is negative, silicon doped by phosphorus is referred to as N-type silicon. [26-31]

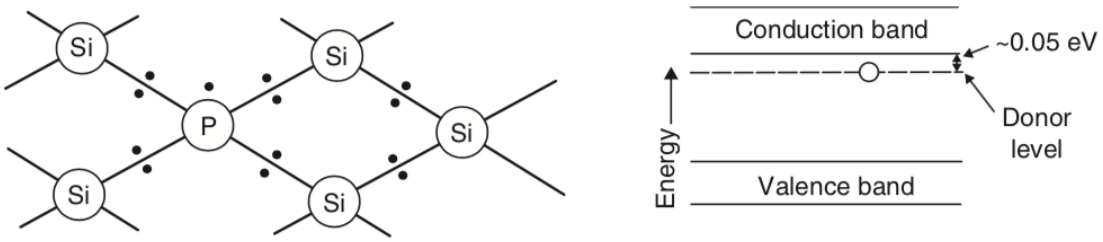

Figure 20: The crystal lattice structure of silicon containing phosphorus impurities along with its energy levels. [30]

On the contrary, when is an atom with three valence electrons such as boron implemented into the crystal lattice structure of silicon, only three bonds will be formed. Since there is no fourth electron to bond with the fourth silicon atom, a so-called electron-hole occurs in the lattice structure as depicted in Figure 21. [26-31]

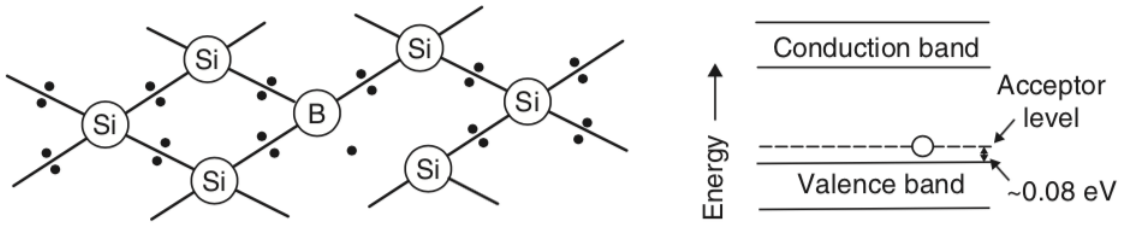

Figure 21: The crystal lattice structure of silicon containing boron impurities along with its energy levels. [30]

Energy levels shown in Figure 21 illustrate a very close gap of approx. 0.08 eV between the acceptor level, i.e. level occupied by electron-holes, and the valence band suggesting relatively easy transfer into the valence band. In principle, electron-holes are also capable of conducting electricity. When an electron migrates in the crystal lattice structure to fill a hole, it leaves another

electron-hole in its original position. Therefore, as electrons move in one direction to fill holes, electron-holes move in the opposite direction. Unlike electrons being negative charge carriers, electron-holes carry a positive charge. Thus, silicon doped by boron is referred to as P-type silicon. [26-31]

Suppose a combination of both previously described types of silicon, i.e. P-type silicon in close contact with N-type silicon forming a so-called P-N junction as shown in Figure 22. In such an arrangement, electrons from N-type silicon will drift across to fill electron-holes from P-type silicon resulting in an area without the presence of electrons or electron-holes and referred to as the depletion region. Additionally, applying positive voltage to N-type silicon and negative voltage to P-type silicon will lead to the increased area of the depletion region since electrons will be pulled by the positive voltage farther from the junction. The area of the depletion region is given by the purity of silicon and the applied voltage. Nonetheless, properties of P-N junction alter after an interaction with incident radiation. The passage of ionizing radiation through the depletion region causes the generation of electron-holes in the valence band and electrons in the conduction band. Electron-holes will drift to the negative charge, i.e. the P-type part, and electrons will drift to the positive charge, i.e. the N-type part, resulting in an electrical signal at the device's output. Hence, the depletion region is a sensitive part of semiconductor detectors. [26-31]

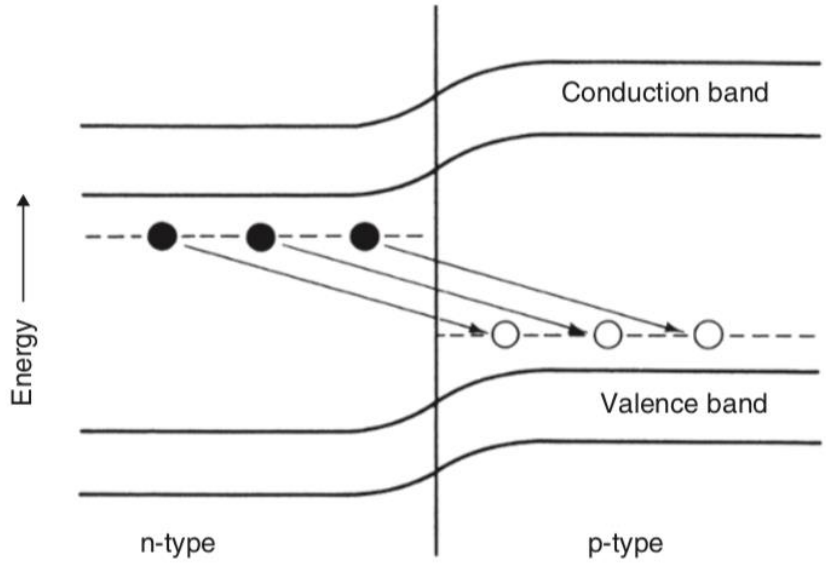

Figure 22: A schematic diagram of P-N junction and illustration of the electron migration forming the depletion region. [30]

Additionally, germanium can also be used as a detector material. Due to its higher atomic number (32) in comparison with silicon's (14), germanium is more likely to interact with gamma rays. Hence, germanium detectors are often being used for the gamma-ray detection. Furthermore, the energy required to generate electron-hole pairs is only 2.9 eV compared to 3.6 eV required by silicon. Thus, the energy resolution of germanium detectors is even better than of silicon detectors. On the other hand, the forbidden gap of germanium is only 0.66 eV. As the result of such a small forbidden gap, electron-hole pairs are generated even at room temperatures due to the thermal excitation. This leads to a significant noise and corruptions of the detection. Consequently, germanium detectors are being cooled by liquid nitrogen to approx. 77 K to avoid this phenomenon. [26-31]

Specific categories of semiconductor detectors vary in the configuration of their P-type, N-type material, forms of P-N junction and based on required properties resulting from specific applications, such as personnel monitoring, spectroscopy of charged particles, high-energy protons or high-energy particles including X-rays and gamma rays. For example, categories of semiconductor detectors include diffused junction detectors, surface barrier detectors, ion implanted layers, fully depleted detectors and passivated planar detectors. [26-31]

The energy required to produce an electron-hole in silicon is approx. 3.6 eV, i.e. approx. three times the forbidden gap energy. Because this energy does not depend on a particle's charge or its mass, semiconductor detectors sense all types of ionizing incident particles. In comparison, the energy to produce an ion-electron pair in gas-filled detectors is approx. 30 eV. Hence, the same energy generates approx. 8 times more responses in semiconductor detectors than in gas-filled detectors. Similarly, the average energy to produce one photoelectron in scintillation detectors is approx. 1000 eV, thus the same energy produces approx. 277 times more responses in semiconductor detectors. More responses per the same energy mean superior energy resolution of semiconductor detectors. Comparison of germanium detector and scintillation detector in terms of their energy resolution is illustrated in Figure 23. In summary, semiconductor detectors are superior as a result of their energy resolution, lower ionization energy and compact size. On the other hand, germanium-based detectors require to be cooled and semiconductor detectors, in general, are more expensive than gas-filled detectors or scintillation detectors. [26-31]

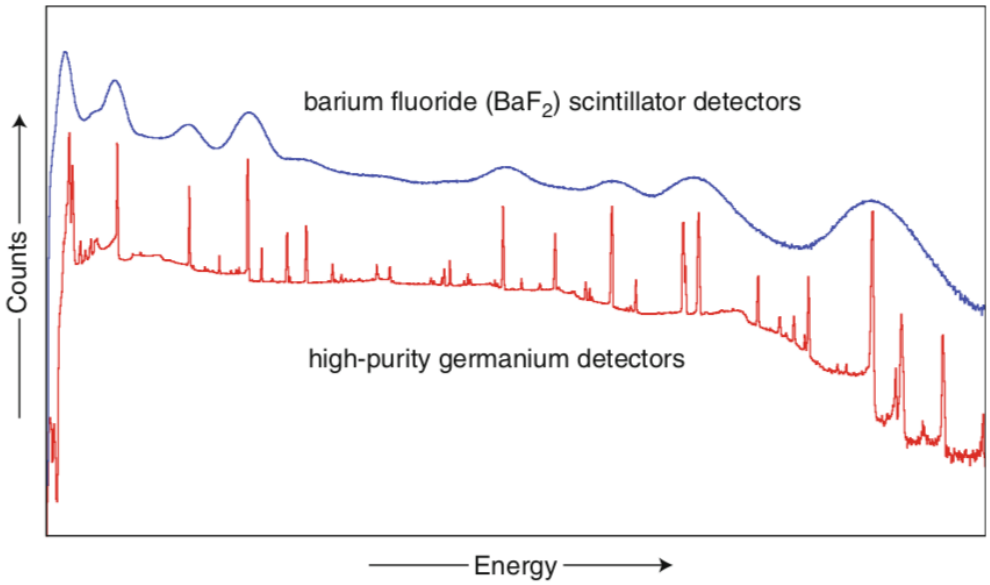

Figure 23: Comparison of germanium detector and scintillation detector in terms of their energy resolution demonstrated on radioactive decay of europium-152. [29]

6.4 Position-sensitive semiconductor detectors

One of many applications of semiconductor detectors are position-sensitive detectors. In this configuration is the position of the interaction of the incident particle sensed along with the particle's energy. Gas-filled detectors are also used for this purpose, but semiconductor detectors are in most applications preferred because of their compactness and their supreme stopping power per unit length. For instance, position-sensitive detectors include resistive or capacitive charge division detectors, microstrip detectors, pixel detectors, drift detectors and charge coupled devices. Pixel detectors are further described since the main subject of this thesis is environmental testing of a pixel-type semiconductor detector. [27]

In general, a pixel in image processing is a picture element. Thus, a pixel detector refers to a device capable of capturing an image composed of a certain number of pixels. Quantity of pixels on specific area or dimension of pixels correlate with the image quality. In case of a pixel semiconductor detector, a two-dimensional position of an incident particle collision with the detector is obtained as the result of implementing electrically isolated pixels into a checkerboard pattern. Electrical connection for each pixel cell along with an individual electronic read-out channel is required. In general, read-out electronics of pixel detectors include an amplifier and a threshold-observing comparator. A pixel cell of such a detector is illustrated in Figure 24. The

usual fabrication approach is to manufacture sensors and read-out electronics separately and then interconnect them. The manufacture technologies include flip-chip solder bonding or indium bump bonds. Pixel detectors constructed through this technique are referred to as hybrid pixel detectors. Additionally, several thousands of detector pixel cells in a matrix of a few square centimetres can be put together due to planar technology integration. [27, 33]

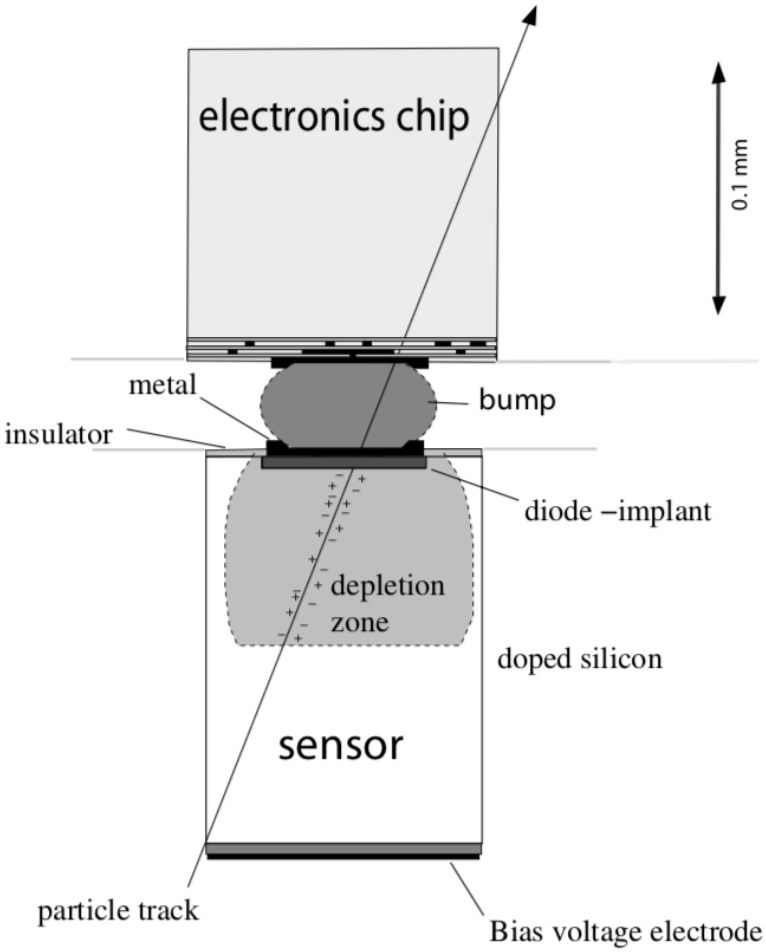

Figure 24: Schematic illustration of an individual pixel cell of hybrid pixel semiconductor detectors. [33]

Due to the frequent use in space dosimetry applications, the family of Medipix pixel detectors composed of Medipix and Timepix variants is described in more detail in the following chapter.

6.4.1 Medipix family of pixel detectors

Medipix is a family of pixel detectors, such as Medipix3, Timepix3 and their older alternatives, developed by an international group of scientists led by CERN. The first chip Medipix1 consisted of a matrix of 4096 pixels on a pitch of 170 μm with an active area of 1.2 cm^2. Each pixel was equipped with a 15-bit counter as an event register. The following detector Medipix2 was developed as a larger chip with smaller pixel cells using 250 nm CMOS technology resulting in 65 536 pixels on a pitch of 55 μm with an active area of 1.982 cm^2. In comparison with its former version, Medipix2 allowed window selectivity due to its 2 threshold limits. Many improved forms of Medipix2 with supreme characteristics regarding temperature stability, pixel counter overflow protections and other augmentations were fabricated. The final version of this detector is referred to as Medipix2MXR. Timepix was developed subsequently as an evolution of Medipix2MXR. While Medipix2 produced a two-dimensional event information based on a threshold-exceeding hits counting, Timepix adds clock ticks counting for each pixel. This technology delivers information regarding three-dimensional tracks of the particle. Moreover, individual pixels can be programmed either to count hits, count clock ticks from the start of the exposition until the termination of the data acquisition defined by the user, i.e. the Time-of-Arrival mode, or count clock ticks from the moment of exceeding the threshold until the same signal crosses the threshold on its downward slope, i.e. the Time-over-Threshold. Described modes of operation are illustrated in Figure 25. Furthermore, individual pixels can be configured independently on other pixels leading to significant versatility of the chip. [34, 35]

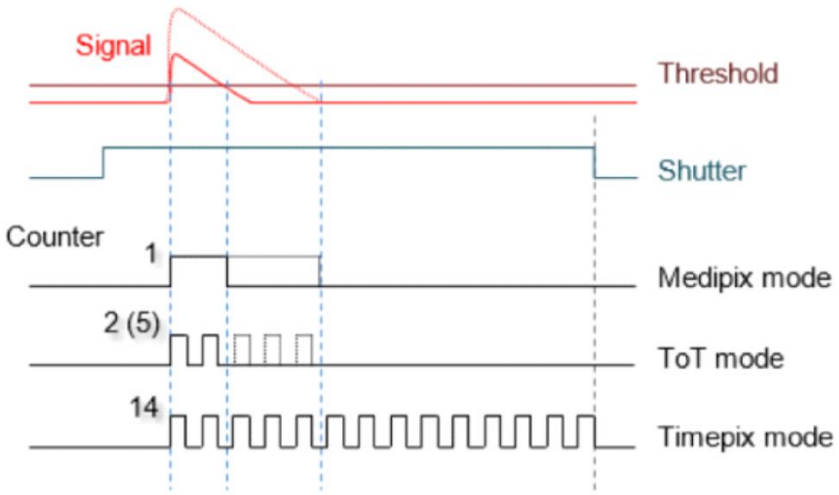

Figure 25: A schematic diagram representing hit counting (the Medipix mode), the Time-over-Threshold mode and the Time-of-Arrival mode (Timepix mode) for two particles of different energy. [36]

The newest Medipix pixel detector called Medipix3 is further improved in terms of CMOS technology, decrease of noise, multiple threshold options and multiple counter registers implementation leading to zero dead time of measurement. Lastly, Timepix3 is an upgraded version of Timepix with a decreased minimum detectable charge, better timing resolution and altered data read-out. Instead of the overall matrix readout, Timepix3 sends values from individual pixels directly after the exposure along with coordinates off-chip. Hence, unlike the sequence of frames produced by former versions, Timepix3 generates a continuous data flow. Timepix3 also permits measurement of the arrival time together with charge deposition information for each individual pixel hit. An example of the outcome from Timepix measurement is illustrated in Figure 26. [34, 35]

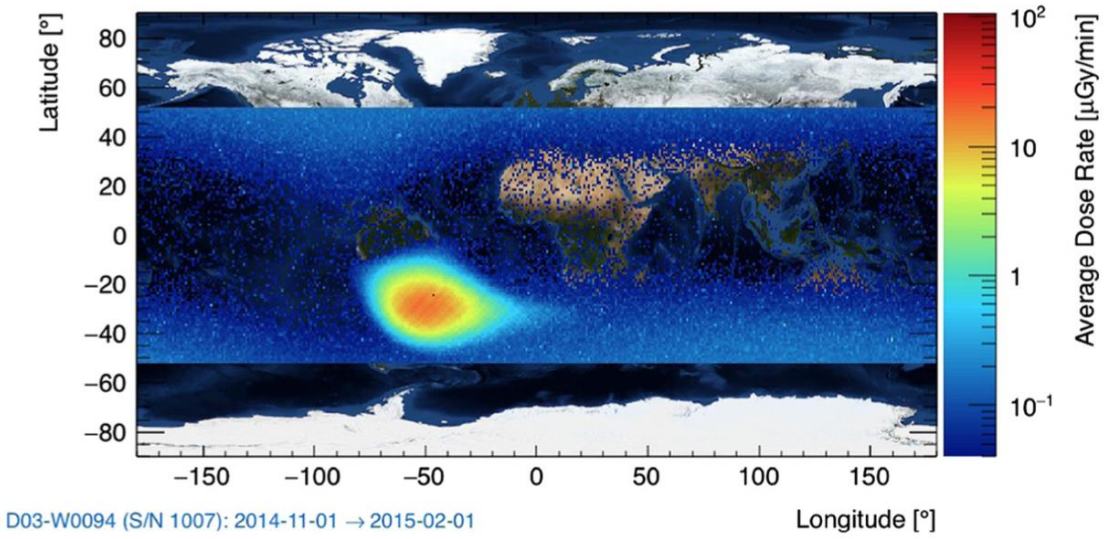

Figure 26: A reconstruction of an image recorded by one of the Timepix assemblies on board of the ISS highlighting the SAA. [34]

6.4.2 The SpacePix pixel detector

Since the topic of this thesis is environmental testing of the SpacePix detector, this detector is described in more detail. The SpacePix is a pixel detector designed for space dosimetry. The detector consists of 64x32 pixels with each pixel on a pitch of 60 µm. Therefore, its sensitive area covers 3840x1920 μm^2. The required supply voltage for the sensor unit is -150 V. The power supply for supplement electronics, such as preamplification, analogue, digital and ADC power domains, is 1.8 V. The detection range of the SpacePix is 5 keV to 36 MeV. [37]

The read-out part contains a charge sensitive logarithmic amplifier with a transfer function and peak detector hold circuit. Consequently, analogue amplitudes resulted from the incident particle interaction with the detector are digitized by an 8-bit ADC and read by either low-voltage differential signalling in the LVDS mode or by single-ended signals in the CMOS mode. The data rate is 10 and 500 Mbit per second for CMOS and LVDS modes, respectively. The CMOS mode is designed for microcontrollers with a maximum data read-out frequency of approx. 10 MHz. The LVDS mode serves if faster data rates are required. This configuration allows communication up to 500 MHz of the clock frequency. However, considering the LVDS mode communication of hundreds of MHz, not only the data-clock but also bit-shift adjustments must be performed in order to compensate the interchip delay time exceeding the clock period. Communication with the SpacePix, i.e. the data acquisition and the chip configuration, is ensured through the on-chip shift register with 512 bits length. Furthermore, the SpacePix in the CMOS mode can be configured through the SPI interface. Simulated transfer function of the SpacePix is shown in Figure 27. [37]

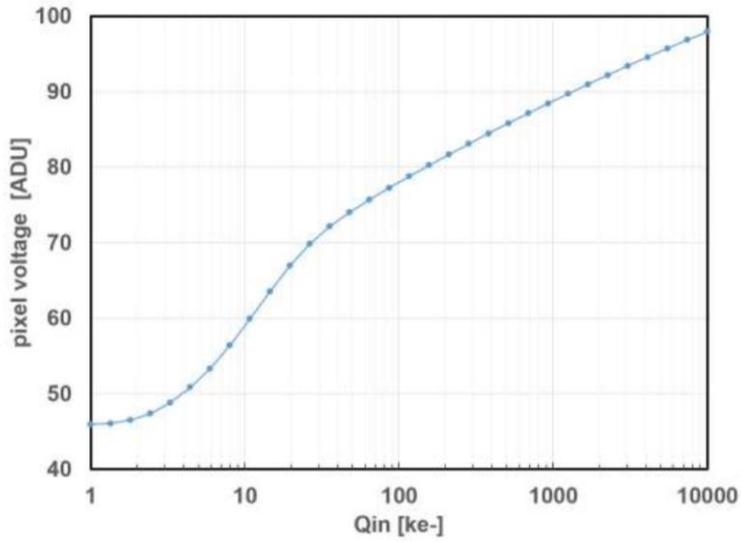

Figure 27: The transfer function of individual pixels of the SpacePix detector. [37]

Accurate power consumption of the chip throughout a practical application is difficult to predict due to the consumption being a function of many variables, such as bias settings, mode of operation, radiation exposure and readout speed. However, some estimations were calculated. The consumption of the preamplifier domain is expected to be 160 µA. Considering the analogue domain, the pixel matrix consumption is estimated to be approx. 47 mA. The power consumption of the digital domain in the LVDS default mode should not exceed 10 mA. Furthermore, consumption of all ADCs is assumed to be approx. 9 mA. Lastly, the bias current consumption is

expected not to top 10 μA. The value of bias current consumption is predicted to be largely influenced by ionizing radiation. [37]

6.4.3 The XChip pixel detector

Since not only the SpacePix detector but also the XChip detector closely relates to this thesis, it is also detailed in this section. The XChip pixel detector is a chip designed for radiation imaging, identification of electrons, protons, heavy ions and advanced radiation dosimetry, i.e. direct LET measurement. A typical application of the XChip detector is space-related monitoring of charged particles for the space situation-awareness purposes. The detector consists of 64x64 pixels with each pixel on a pitch of 60 μm. Thus, its sensitive area covers 3840x3840 μm^2. The sensory unit requires -100 V, whereas the voltage supply for supplement electronics is 1.8 V. The detection range of the XChip is 5 keV to 30 keV. [38]

In general, the detection of radiation with the XChip is possible in two modes, i.e. the hit counting mode and the ADC mode. In the hit counting mode, only hits with energy exceeding the user-defined threshold are taken into account by a 16-bit counter. This mode is primarily designed for radiation imaging. The ADC mode's purpose is to measure the deposited energy in individual pixels and as the result to identify the incident particles. The data exchange is possible in two modes, i.e. the CMOS mode and the LVDS, and with the same characteristics as depicted for the SpacePix detector except for the LVDS data rate and the shift register. The upper limit for the XChip's LVDS mode is 400 Mbit per second instead of 500 Mbit per second data rate of the SpacePix LVDS mode and the on-chip shift register of the XChip is 1024-bits long. [38]

Power consumption is also estimated for the XChip detector with the same uncertainty due to the consumption being a function of many variables as in the case of the SpacePix detector. The analogue domain is expected to be consuming approx. 17 mA. The digital domain and all ADCs are estimated to consume approx. 33 mA and 5 mA, respectively. The XChip bonded to a PCB is shown in Figure 28. [38]

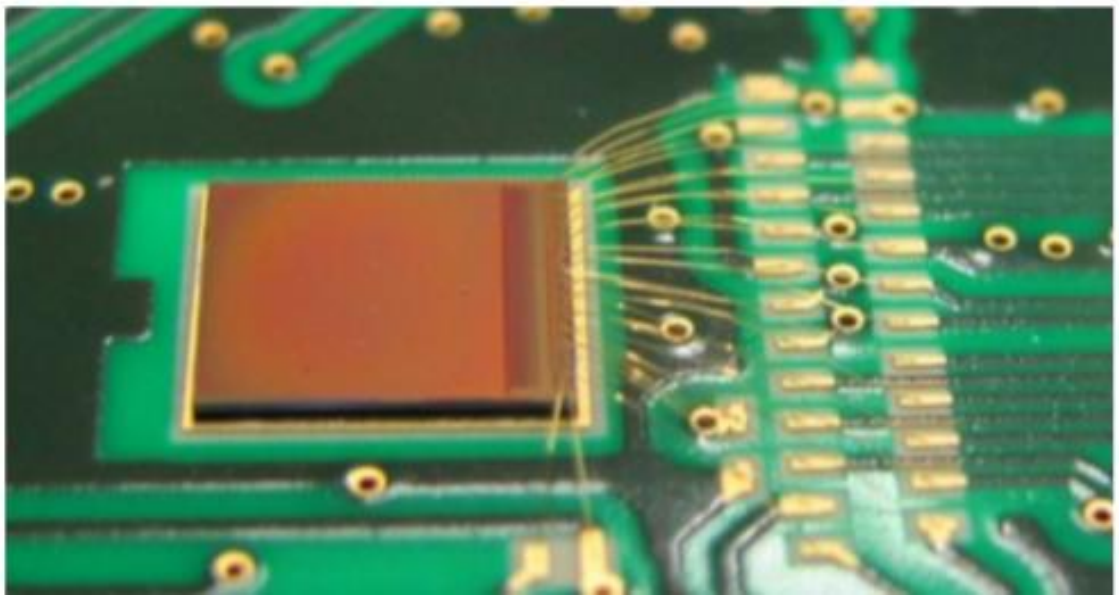

Figure 28: The XChip pixel detector bonded to a PCB. [39]

7 Necessary hardware characteristics for space applications regarding the space environment

Since not only radiation but also other aspects of the space environment contribute to requirements and the load on hardware parts of spacecraft, individual components of the space environment are characterized in the first place. The description of ionizing radiation is omitted as it was depicted in the previous chapters. Furthermore, hardware can be divided into mechanical or electrical parts and its necessary characteristics studied on both. However, because of the topic of this thesis, the main emphasis in this chapter will be on the description of hardware characteristics resulting from the mitigation of ionizing radiation effects. Other environmental aspects and mitigation strategies are also briefly described.

7.1 The space environment and mitigation strategies

Vacuum is a term of wide comprehension. In general, it is a region of much lower pressure than the atmospheric pressure. However, it can be further divided into several types, such as rough, medium, hard or extreme vacuum, ranging from 10^{3} to 10^{-15} Pa. Even cosmic vacuum varies this significantly since it depends on altitude. For example, at an altitude of approx. 100 km, i.e. so-called boundary of outer space or the Karman line, is the pressure in the range of 1 to 10^{-3} Pa. Farther increase in the altitude to approx. 400 km leads to a decrease of pressure to values of 10^{-5} to 10^{-7} Pa. Additionally, pressure values outside the solar system can reach up to 10^{-15} Pa. Based on individual material characteristics, vacuum values of pressure may cause a so-called outgassing. The outgassed molecules of a material are then accumulated on the proximate surface. This phenomenon is dangerous especially for sensitive optics or solar panels and may result in loss of performance or efficiency. To mitigate this problem, designers must take into consideration vacuum-exposed areas, operating temperature range, present a list of all materials used, review this list periodically and compare the materials with databases such as ASTM E1559 containing experimental results. If an unsuitable material occurs in a region exposed to a vacuum and is known to outgas, it should be so-called thermally baked at a temperature exceeding the predicted temperature in orbit in a vacuum of at least 10^{-2} Pa and for at least 24 hours. For instance, detailed specifications to achieve an acceptable level of outgassing through the thermal vacuum bakeout are described in NASA's MSFC-SPEC-1238 standard. [40, 42]

Another space environment component is atomic oxygen originating in the upper atmosphere due to the interaction of atmospheric oxygen with UV radiation. Atomic oxygen causes severe oxidation and plays a major role in material degradation especially at altitudes from 150 to 600 km. Mainly metals undergo erosion due to the presence of atomic oxygen, such as silver or copper. Also, polymeric materials containing carbon, nitrogen, sulphur and hydrogen bonds erode. Furthermore, the fluence of atomic oxygen is not only influenced by the altitude of flight and spacecraft orientation but also by the solar cycle. The solar maximum corresponds to larger fluences of atomic oxygen and vice versa. Degradation of solar panels is illustrated in Figure 29. To mitigate erosion of coating materials induced by atomic oxygen, standard guidelines for the coating materials selection should be followed such as NASA/TP 1999-209260. More standards such as ASTM E2089 are used for testing purposes of a variety of materials reactivity to atomic oxygen. Moreover, the consequence of the presence of the atmosphere is not only degradation of materials but also the contribution to drag resulting in torque and orbital decay. The amount of drag depends on the solar cycle in the same manner as in the previous case. [40, 43]

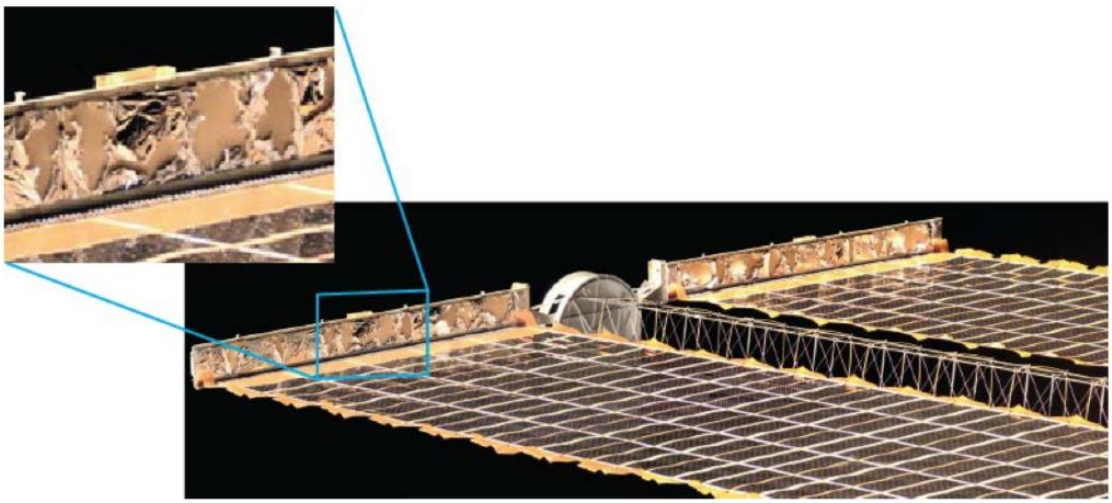

Figure 29: Degradation of solar panels on the ISS caused by atomic oxygen after 1 year of the space environment exposure. [40]

UV radiation is also responsible for direct degradation of materials. Polymers, such as polycarbonate or fluorinated ethylene propylene, are damaged by UV either by a so-called cross-linking or chain scission depending on the wavelength of irradiation. In general, UV radiation also alters the colour of the material and usually darkens it as shown in Figure 30. Therefore, it also alters properties of the thermal coating by increasing absorptivity. Potentially suitable materials for the UV radiation exposure are being tested along with the ability to withstand the exposure to atomic oxygen since degradation caused by these two aspects of the space

environment is closely related. For instance, such a versatile coating material considered very promising is polybenzoxazole. [40, 44]

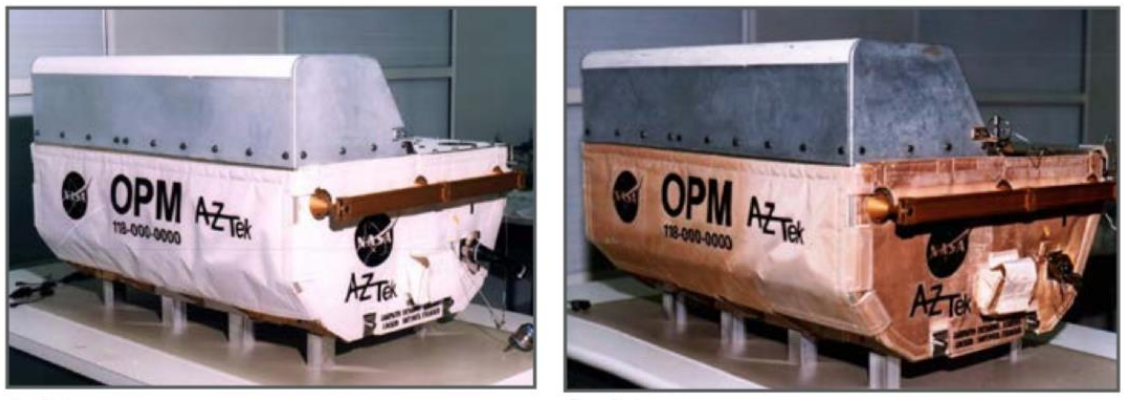

Figure 30: Degradation of the Optical Properties Monitor after 9 months of the space environment exposure on the Mir Space Station caused by UV radiation (pre-flight on the left, post-flight on the right). [40]

The solar activity and the altitude of orbit also determine the amount of positively charged ions and negative electrons, i.e. the amount of plasma surrounding spacecraft. However, these ions and electrons are not distributed equally on a spacecraft's surface. In general, ions can only impact leading edge surfaces, unlike electrons with the ability to reside on any surface of spacecraft. Consequently, unequal distribution leads to charging, parasitic currents, electrostatic discharge or ion sputtering. Design guidelines serving to mitigate charging effects caused by the surrounding plasma environment are written by space agency. In general, these control methods can be categorized as either active and passive or electron ejecting and ion receiving. Combination of all methods is recommended. These methods include sharp spikes, electron and ion emission methods, the use of conducting grids or partially conducting paints. [40, 45]

Periodic orbiting of a satellite around its primary body causes periodic changes in the illumination of spacecraft's surfaces. An exception might occur considering a mission outside the solar system. Nonetheless, considering the most probable scenario of a satellite orbiting the Earth, materials of a spacecraft's surface experience thermal cycling to a various degree depending not only on the duration of the Sun's exposure but also on its material characteristics, such as absorptance and emittance, orientation of the spacecraft to the Earth and the Sun or the amount of heat produced by the spacecraft itself. Usually considered thermal cycling for a LEO satellite is -120 °C to 120 °C. For instance, hardware manufactured from materials with poor thermal properties might exceed the temperature limit for astronaut's gloves and become inoperable. Moreover, hardware

composed from multiple materials with various coefficients of thermal expansion might be damaged due to temperature changes. Mostly coating materials experience thermal cycling and subsequent degradation. Consequently, degradation of coating materials might expose underlying layers to atomic oxygen and cause further damages as shown in Figure 31. Therefore, coating surfaces should be composed of materials with similar coefficients of thermal expansion. For instance, a list of suitable materials for various coating, tapes or solar cells tested for solar absorptance and emittance together with the description of the testing procedures is NASA/TP 2005 212792 document. [40, 46]

Figure 31: Outcomes of the ISS Material experiment 4 illustrating the failure of the coating resulting from the combination of thermal cycling and the exposure to atomic oxygen. [40]

Finally, the space environment is also composed of micrometeoroids and orbital debris. Micrometeoroids can damage spacecraft due to their high velocity ranging from 10 to 70 km/s. The fluence of micrometeoroids in the proximity of the Earth varies based on their size and can be approximated through a variety of models such as the Space Environment Information System by ESA. Moreover, regular increases in the fluence of micrometeoroids are induced by flybys of comets. Orbital debris usually travels at an average velocity of 10 km/s. Large space debris can be tracked in order to avoid collisions through safety manoeuvres performed by satellites. However, the majority of space debris is too small to be tracked and poses a danger especially for surfaces in the direction of the satellite's motion. The amount of space debris is also influenced by the solar cycle through atmospheric heating and increased drag. Micrometeoroid or debris collisions in LEO were studied on NASA's Long Duration Exposure Facility (LDEF) from 1984 to 1990. During its almost 6-year exposure to the space environment, LDEF recorded one impact of approx. 0.7 mm in diameter causing a 2.5 mm deep penetration into aluminium wall on its 7 m^2 testing area in the direction of the satellite's motion. Furthermore, one impact per m^2 of a 1.5 mm

deep penetration was experienced on the same testing area. However, the current fluence of impacts is expected to be larger due to the increased amount of debris in LEO. For instance, China's test of an anti-satellite missile in 2007 resulting in destruction of the Fengyun 1-C spacecraft in LEO and collision between the Iridium 33 and the Cosmos 2251 satellites in 2009 increased the number of small untraceable debris by 250 000 or more. Obvious methods to mitigate micrometeoroid/space debris hazard are to minimize the probability of being hit, minimize the probability of a possible shortcut should an impact occur and protect sensitive electronics behind as much shielding as possible. In case of meteor showers, it is possible to orient solar panels in the parallel direction, orient sensitive optics away from the direction of the meteor stream arrival or shut down all electronics in the possible penetration depth. Furthermore, new concepts of effective low mass shields are emerging such as protecting spacecraft using a honeycomb of small gas-filled containments. [40, 47-49]

Lastly, weightlessness or zero-g is an important aspect of the space environment. However, in missions related to orbiting the Earth or possible Mars endeavours, the gravity is only reduced and rather than zero-g it is referred to as microgravity. Its effect is being considered mainly in terms of the effect on living organisms and especially humans in various means or in terms of change in physical and chemical properties, e.g. resulting conditions of fuel during take-off and the need of acceleration to provide the fuel to engines. [41]

7.2 Mitigation of hazard to electronics induced by ionizing radiation

The space environment in terms of ionizing radiation is described in chapter 3. Hazard to electronics caused by ionizing radiation is depicted in chapter 4. Given the effect of ionizing radiation on electronic hardware, the need for mitigation techniques is obvious. Methodology ensuring functionality and proper performance of electronic hardware in the ionizing radiation environment is called the radiation hardness assurance. Necessary hardware characteristics required for adequate operations in the radiation environment are the outcome of this assurance. [50]

The radiation hardness assurance consists of system requirements, environmental definitions, part selection and testing, shielding and radiation tolerant design. Since mission specifics, requirements on parts or payload can change during the lifetime of a mission's design, the process is iterative. It starts with a description of the predicted mission radiation environment and resulting

exposure levels. These levels relate to estimated TID of each part calculated from mission specifics, particles spectra, LET and dose-depth curve of shielding. It follows with an evaluation of individual part's radiation sensitivity based on data from appropriate databases or radiation tests. Furthermore, the part's radiation sensitivity together with degradation of performance over the mission's duration is used for the worst-case analysis of systems and circuitry. The outcome is the radiation failure level for each part. Finally, the part's failure level is compared with exposure levels and the part is then categorized based on its Radiation Design Margin (RDM). RDM is a ratio of the part's failure level to the exposure level. If RDM of a part is greater than 1, it is not hardness critical and can be used without any restrictions. When RDM of a part is lower than 1, one option is to perform more accurate tests in order to increase the precision of TID estimate. Another option is to implement countermeasures to reduce requirements on the part, such as additional shielding, application of error correction systems, protection circuitry, etc. The third option is to replace the part by another one with higher RDM. Finally, the part can also be considered hardness critical if its RDM is not significantly greater than 1. Given the small variations between the same parts caused by inaccurate manufacturing, RDM of parts from the same lot can vary and, in some cases, even lead to RDM lower than 1. Therefore, these parts are tested too. The two most important steps are defining the radiation environment and defining the part's failure level. Hence, these two steps are described in more detail. Decreasing components radiation sensitivity is also covered in this section. Finally, the disadvantages of radiation-hardened components and further options are described. [50]

7.2.1 Defining the radiation environment

The radiation environment can be defined by studying the external radiation environment surrounding spacecraft throughout its mission duration and by studying its effects reflected as the internal environment within the spacecraft. Both are described in the following paragraphs. [50]

LEO is characterized with an altitude of 300 to 2000 km. Ionizing radiation is not equally distributed in this region because of Van Allen belts. Passing through high latitudes means experiencing the presence of the outer belt and lack of the Earth's magnetosphere. The South Atlantic region poses danger due to the presence of trapped particles of the inner belt. All in all, low equatorial orbits of an altitude of approx. 300 km sustain little ionizing radiation. LEO satellites with inclination lower than 45 ° are endangered by the SAA and experience ionizing radiation of approx. 1 gray per year. LEO satellites with inclination higher than 55 ° are endangered by both the outer belt and the SAA and experience approx. 10 gray per year. LEO satellites at greater altitudes, e.g. 1500 km, are subjected to the inner belt and sometimes

experience the same ionizing radiation as Geosynchronous Earth Orbits (GEO) of 100 gray per year. [51, 52]

Medium Earth Orbit (MEO) is located at altitudes ranging from 2000 km to 35 786 km and is subjected to harsh ionizing radiation due to the presence of Van Allen belts. However, satellites are usually placed in orbits between the two belts in order to minimize their influence. Even though the particle density between the belts is lower, it changes randomly because of the solar cycle effects. Ionizing radiation doses in these orbits are approx. 1000 gray per year. [51, 52]

GEO is located at an altitude of 35 786 km. Spacecraft in this orbit experience ionizing radiation due to the presence of the outer belt, SPE and GCR. Ionizing radiation doses in this orbit are approx. 100 gray per year. [51, 52]

Doses for orbits with high eccentricity, such as Highly-Elliptic Orbit (HEO) or Geo-Transfer Orbit (GTO), vary significantly based on the altitude, exact eccentricity and solar conditions. Furthermore, all previously described orbits are passed by spacecraft during the flight in HEO and GTO. Estimations for HEO are of the order of 100 gray per year and for GTO are of the order of 50 gray per transit. [51, 52]

Mars-orbiting missions or Mars surface missions would experience the major part of ionizing radiation dose throughout their arrival. Since there are no radiation belts around Mars due to its weak magnetic field, SPE and GCR is the main concern. Spacecraft orbiting Mars would be subjected to approx. 10 gray per year of ionizing dose. [51, 52]

A deep space mission's main dose of ionizing radiation is caused by GCR. SPE would also be experienced. However, the intensity of SPE decreases as $1/r^2$ with the distance from the Sun. A dose of 200 gray per year is usually considered. Moreover, deep space missions or long-duration missions, in general, would experience ionizing radiation originated in spacecraft's Radioisotope Thermoelectric Generators (RTG) should this power source be used. Nonetheless, the dose originated in RTG is in most cases negligible. [51, 52]

Specific values stated above are considered for a 2.54 mm thick aluminium shielding and based on calculations and experience from numerous missions. Since the dose highly depends on shielding geometry, precise altitude and inclination, the values are a rough estimate. Additionally, not only orbital parameters but also the worst-case number of orbits, i.e. the worst-case duration of a mission or the solar cycle at the time of the mission, is being considered for the estimation of

the radiation conditions. In addition to the empirical data, models for trapped radiation belts, SPE and GCR are available for the radiation conditions estimation. [50-52]

Estimation of the internal radiation environment is required to be as precise as possible. Overspecification leads to additional costs and underspecification leads to endangerment of the mission. TID and displacement damage effects are considered for the quantification of electronic components degradation, material degradation, optoelectronic components and solar cells degradation. Ions LET and proton energy spectra are necessary for the SEE determination. [50]

TID is calculated in terms of spacecraft shielding. This process is rather complex and comprises of a few steps. After the flux spectra are determined based on mission specifications and radiation environmental models, the radiation transport analysis is performed either by using relatively simple three-dimensional sector based codes or more complicated three-dimensional Monte Carlo transport codes. Furthermore, the dose depth curve is calculated based on SHIELDOSE model formed from a large data set containing radiation doses as a function of shielding and particles energy. The dose depth curve provides the ionizing radiation dose as a function of either the shield thickness in planar geometry or as a function of spherical shielding around a point. The planar representation is used for parts near the surface of spacecraft and the spherical representation is used for the rest. An example of a dose depth curve is shown in Figure 32. [50]

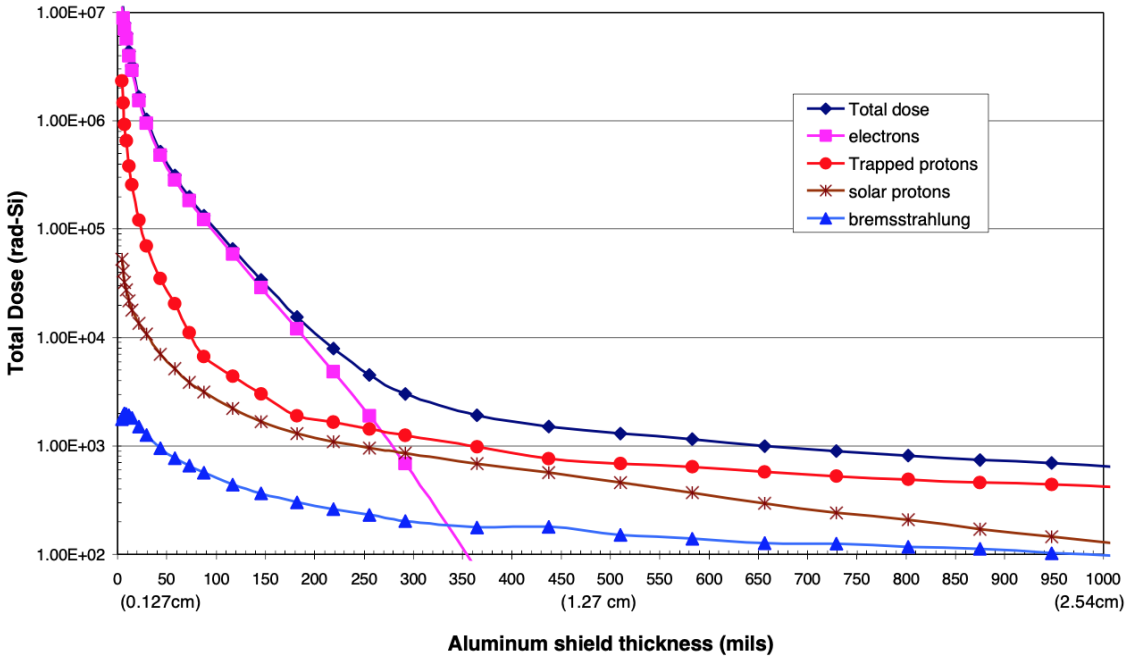

Figure 32: TID at the centre of an aluminium sphere of various thickness of the ST5 mission (HEO, altitude ranging from 200 to 35 790 km, three months duration and 0 ° inclination). [50]

Additionally, the sector-based analysis is performed. Input to this analysis is the dose depth curve and three-dimensional model of the part's surroundings. The outcome is TID causing the part's destruction. [50]

SEE are investigated through studies on heavy ion LET and proton spectra considering a certain value of aluminium shielding, for example, NASA and ESA are assuming 2.54 mm or 3.7 mm, respectively. An example of GCR and SPE spectra are shown in Figure 33. Shielding thickness does not have a significant impact on the GCR fluxes and protons of energy higher than 30 MeV. However, it has an impact on SPE fluxes. Furthermore, protons from radiation belts need to be taken into account. Thus, SEE worst-case analyses must count with peak fluxes induced by passages through radiation belts. [50]

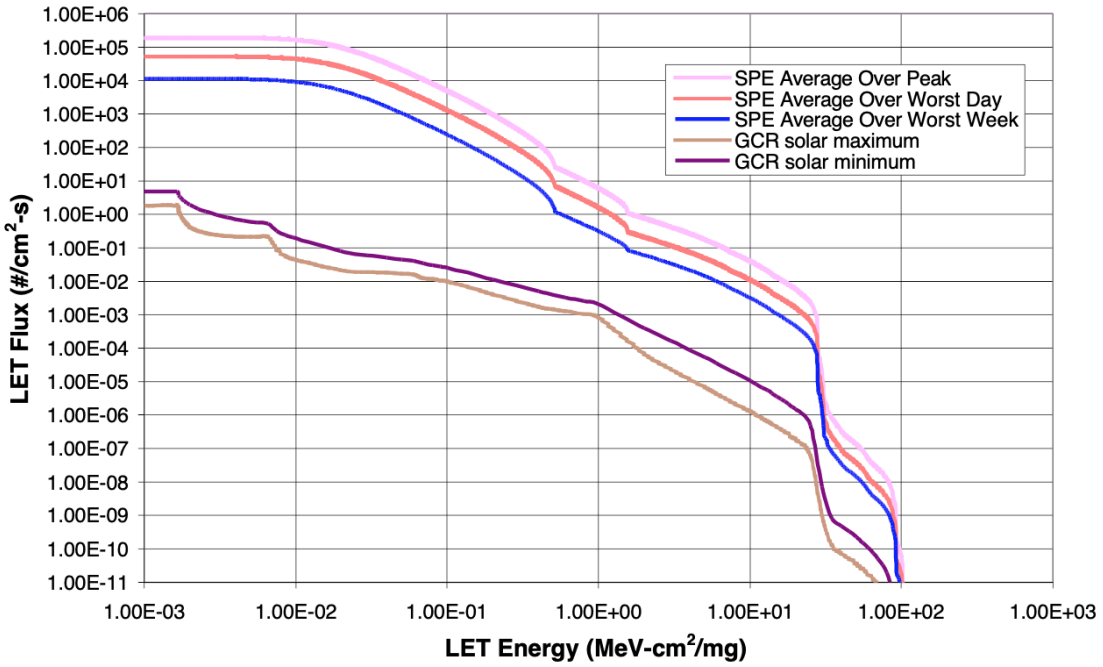

Figure 33: Integral LET spectra in 1 AU distance for interplanetary orbit considering 2.54 mm aluminium shielding. SPE fluxes are significantly higher than GCR fluxes. [50]

Displacement damage effects in the space environment are mainly caused by protons. However, since the coating of solar panels is only approx. 30 μm glass, the electron contribution must also be considered in the case of the degeneration analysis of solar cells. In general, the subjective value of aluminium shielding is considered, e.g. 2.54 mm, and based on predicted fluxes of relevant particles is the displacement damage estimated. If there is a requirement for more accurate calculation, the concept of Non-Ionizing Energy Loss (NIEL) can be used. Particle-induced displacement damage effects are linearly proportional to NIEL. NIEL rates are available

in databases containing values for different target device materials, electrical parameters, particle types and energy. Furthermore, models based on damage coefficients are applied in most cases, such as EQRFRUX-Si and EQRFRUX-Ga. These models even include coefficients for multi-junction solar cells. [50]

7.2.2 Defining the part's failure level

Defining the failure level of analysed parts is the second most important step throughout the radiation hardness assurance as it is used for the RDM calculation. The failure level relates to the part's functionality limits. These limits correspond to an assurance of proper operation of the part throughout the mission's duration. [50]

The definition itself consists of two steps. At first, the circuit analysis is performed in order to establish the exact parameter limits for the part. The part with these limit parameters must still be able to function properly within the circuit. Consequently, the radiation data specifying the performance of the part for specific levels of radiation are taken into account and combined with the circuit analysis to define the radiation failure level. Worst-case scenarios, i.e. the worst possible radiation, temperatures and ageing of the part, are considered. Hence, the part's failure level corresponds to the functionality in the most possible stressful conditions. Figure 34 demonstrates the degradation of the offset voltage of an operational amplifier PM155 depending on the total dose. Eight parts from the same lot were tested and are represented in Figure 34 by different colours. Figure 34 also illustrates the change in the radiation failure level if the acceptable limit for the design is changed. In the case of 2 mV of an acceptable level, the failure level is approx. 40 krad. In comparison, if the acceptable level is reconsidered to the value of 4 mV, the failure level is approx. 75 krad. Lastly, the same components from the same lot have slightly different characteristics as is also shown in Figure 34. [50]

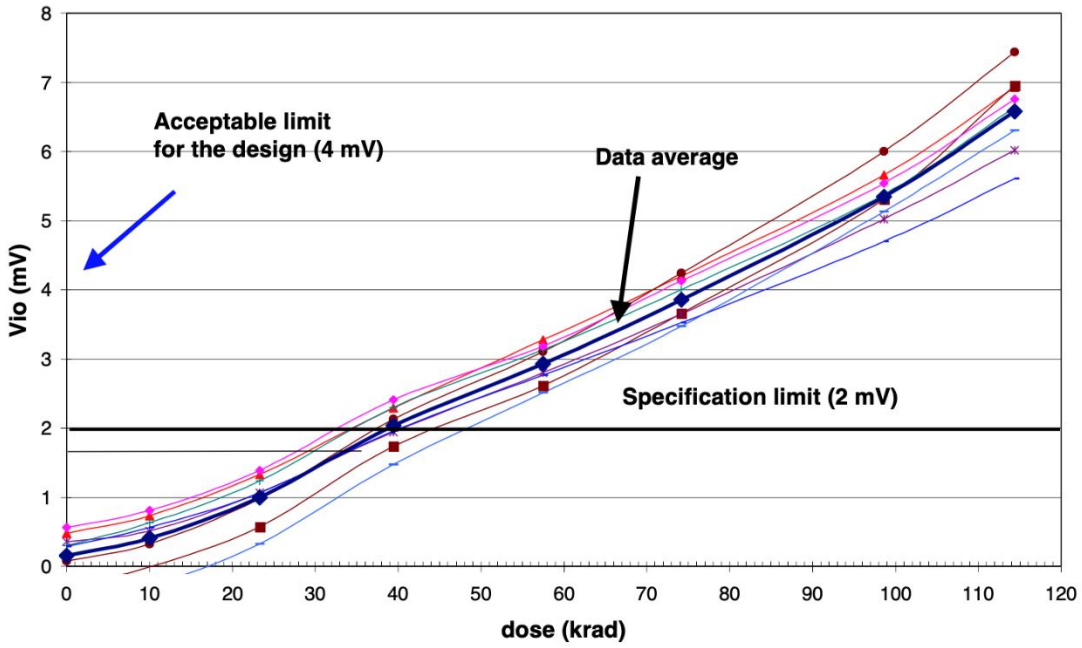

Figure 34: The offset voltage of an operational amplifier PM155 as a function of the total dose. [50]

7.2.3 Techniques for the increase of radiation tolerance

When the radiation hardness analysis of a specific part results in RDM lower than 1, further course of action is to either run more accurate analysis, apply countermeasures or select a different component with lower radiation sensitivity. Components with low radiation sensitivity are so-called radiation-hardened. In general, there are two categories of radiation-hardening techniques, i.e. physical and logical techniques. Physical techniques comprise of insulating substrates usage, bipolar integrated circuit usage, radiation-tolerant SRAM, wide band gap substrate, use of depleted boron and also transistor layout altering techniques. Logical techniques consist of error correcting memory, redundancy usage and watchdog timers. These techniques are detailed in the following paragraphs. [53]

Instead of a usual semiconductor wafer, insulating substrate techniques are often used to manufacture radiation-hardened chips, such as the Silicon On Insulator (SOI) or the Silicon On Sapphire (SOS). In case of the SOI, a layered silicon-insulator-silicon substrate is used instead of a conventional silicon substrate leading to a configuration with silicon junction above an electrical insulator. The SOI configuration's benefits include lower parasitic capacitance as the result of isolation from the bulk silicon and the resistance to SEL as the result of total isolation of N-well

and P-well structures. However, the manufacturing costs are higher compared to conventional silicon-built devices due to increased substrate costs. The SOS technology represents a thin layer of silicon grown on a sapphire wafer. Since sapphire is a great electrical insulator, parasitic currents induced by radiation are not able to spread to surrounding circuitry. Its intrinsic resistance to radiation is a reason for many aerospace and military applications. Nonetheless, since sapphire is costly and fabricating small SOS transistors is complicated due to their higher mass in comparison with the conventional ones, the manufacturing process is very difficult and expensive. In general, SOI and SOS chips can withstand many orders of magnitude greater ionizing radiation in comparison with commercial chips. [53]

Bipolar integrated circuits containing bipolar junction transistors are being used because their radiation tolerance is in principle 100 or even 1000 times higher than CMOS circuits. The reason behind their high radiation tolerance is the vertical construction leading to the collector junction isolation. Additionally, leakage currents between collector and emitter are prevented by avoiding oxide generation. [53, 54]

Radiation-tolerant SRAM is often used instead of DRAM technology. TID effects and SEE are reduced by using epitaxial wafers and self-aligned silicide in order to reduce the resistivity of the drain, source and poly gate. [53, 55]

The advantage of wide band gap substrate materials lies in their supreme characteristics. They are reported to have great power and low noise capabilities, radiation insensitivity and high temperature and frequency insensitivity. Such wide band gap materials, i.e. wide band gap semiconductors, include gallium nitride or silicon carbide. They are defined by small atoms and strong electronegative bonds. This leads to a band gap approx. 2 or 3 times bigger than the band gap of conventional semiconductors. However, as in the previous cases, the manufacturing is difficult and still a subject to development. [53, 56]

Radiation hardening techniques also include the use of depleted boron, i.e. boron-11, instead of boron-10 in the passivation layer. Boron-10 semiconductors are subjected to current leakage into nearby electronics or to SEE in general. Semiconductors with boron-11 do not undergo this process. Therefore, they are more immune to radiation. [53, 57]

Radiation hardness ensured by the change in transistor layout design is of two variants. These variants are so-called enclosed layout transistor and guard ring. Similar configurations to enclosed layout transistor are also ringed source and inter-digitated design layout. All three configurations aim at preventing current leaking between source and drain and as a result aim at preventing TID-

induced effects. SEL can be mitigated by the implementation of so-called guard ring. Guard rings prevent the formation of low resistance path between drain supply and source supply leading to high current flows and component damages by increasing the distance of the adjoining transistors. In principle, guard ring is either heavily doped P-type or N-type semiconductor for negative-type MOS and positive-type MOS, respectively. The downside of this method is the decrease in circuit density. Schematic illustrations of the enclosed layout and guard ring configurations are depicted in Figure 35. [58]

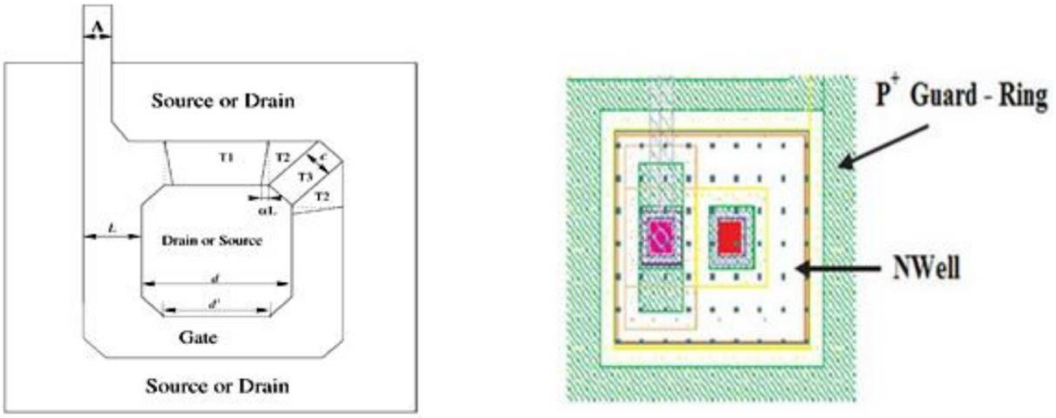

Figure 35: Schematic representation of enclosed layout transistor configuration (on the left) and guard ring configuration (on the right) [58]

Error correcting memories, i.e. error correcting codes or error detection and correction, use is a logical radiation mitigation method. In this technique, neighbouring bits that would possibly suffer from irradiation and upset are assigned to different words and additional parity bits are implemented. This approach allows to recognize and correct the corrupted data. Furthermore, the inspection of RAM must be periodic because irradiation can corrupt the data at any moment and not only in the event of reading. Nonetheless, the cost of implementing error correcting techniques is the computational expense. [53]

Redundancy is another technique for mitigation the radiation-induced effects. Components subjected to SEE are doubled or even tripled and their performance is compared. If an error occurs in one component, the two redundant components outvote the first one and forbid the error to be passed further. This approach is effective since the probability of the exact same error in two components is very low. However, redundancy of elements leads to occupation of more area, bigger computational and power demands and higher price since the redundancy might be in terms of entire microprocessor boards. [53]

Watchdog timer techniques are considered the last possibility regarding radiation hardness techniques. The basic principle of operation is to set a timer and periodically postpone the timer in case of proper operation of the system. If a radiation-induced error occurs, the microprocessor will not be able to send the exact command to the timer in order to postpone it. Therefore, the timer will run out and the system will be hard-restarted. This approach ensures that an errored system will not perform unwanted actions. Additionally, advanced configurations with multiple timers were introduced to improve system recovery. [53]

7.2.4 The disadvantages of radiation hardening and the use of COTS components

The purpose of this chapter is to demonstrate that not only expensive radiation-hardened components but also Commercial Off The Shelf (COTS) components can be used in space applications. The use of COTS components is a possibility emerging from the radiation hardness assurance analysis. This possibility is becoming more popular due to increased requirements on electronic components in space applications, such as mass production and fast access to new technologies.

At first, there are several reasons for not using radiation-hardened components. Except for greater costs related to complicated fabrication, periodic quality examinations must be performed, such as designed radiation dose resistance tests or latent defects inspections. Furthermore, radiation-hardened components are late behind the present-day technology in terms of integration and maturation. However, the biggest reported problem is the long lead time and low density leading to difficulties in design process and poor performance. Radiation-hardened components are appropriate and necessary for certain missions or applications, such as high altitude orbits, deep space missions, ATLAS detector in CERN, etc. However, some applications allow the use of a different approach for radiation effect mitigation. [59, 60]

Instead of the risk avoidance methodology reflected as radiation hardening of components, the risk management methodology is an option. This methodology comprises of the use of COTS components with proven radiation tolerance required for a specific mission. Although the COTS components were not designed to be radiation resistant, they can withstand a certain level of radiation especially with the help of logical radiation hardening. In general, some COTS parts can withstand 10 krad but some cannot withstand 1 krad of ionizing radiation. Therefore, the individual part’s tolerance is proven by tests in terms of system design and system performance under the predicted environment with a reasonable assurance margin. Since the manufacturing

process is usually imperfect, a crucial part of the radiation tolerance examination is also the lot control. In principle, implementation of radiation tolerant COTS components into mission design in comparison with radiation-hardened components is more convenient in terms of performance, availability, costs and lead time. [59, 60]

8 Environmental testing methods

8.1 TMP100 and TMP461 vacuum-compatibility test

Firstly, precise temperature measurement of the PCB containing the SpacePix detector is required for proper thermal testing of the SpacePix. However, it was empirically observed that the previously used temperature sensor TMP100 performs read-out fluctuations of approximately ± 10 °C in vacuum conditions. The reason for poor measurement quality of TMP100 was not entirely clarified. Hence, TMP100 was not discarded but rather analysed in comparison with TMP461, a temperature sensor hardened for space operation. In order to properly measure the temperature of the SpacePix inside the thermal vacuum chamber throughout the environmental testing, temperature sensors TMP100 and TMP461 were tested in the first place.

8.1.1 Common PCB design

As the result of both devices being able to communicate via the I^2C bus, a common PCB for TMP100 and TMP461 was designed. Because Altium designer was not available for free for study purposes at the time, other EDA software were compared. Although KiCad was found to be the best free EDA software solution, EasyEDA tool was selected for its user-friendly environment, low storage requirements and the option of exporting both PCB and schematics design to Altium format files which might be useful in case of using the design for further purposes.

Both TMP100 and TMP461 were installed on the same PCB according to the I^2C address selections and suggestions in datasheets with approx. 2 cm separation to prevent thermal influence. A 4-pin header was added for data and clock lines for the I^2C, as well as ground and power supply. For satisfying both TMP100 and TMP461, +3.3 V was selected for the power supply. The schematics and PCB design are shown in Figure 36 and Figure 37, respectively.

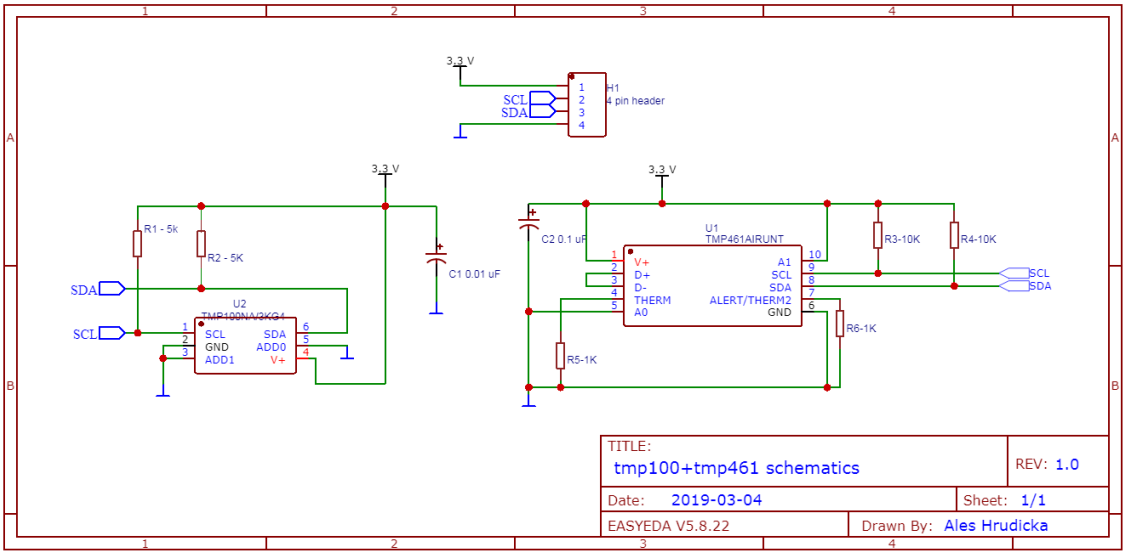

Figure 36: A schematic diagram of TMP100 and TMP461 common PCB.

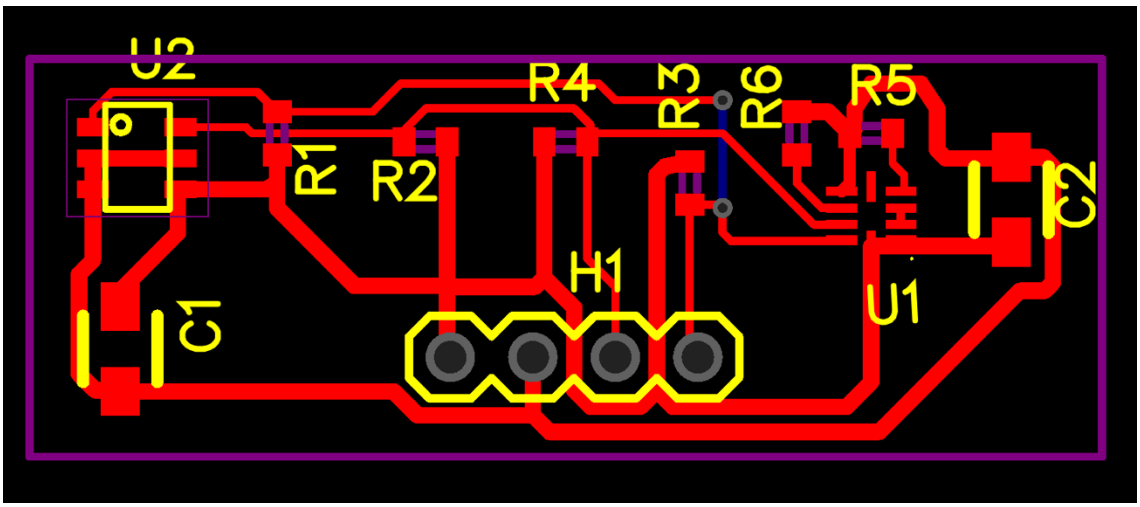

Figure 37: A PCB diagram of TMP100 and TMP461 common PCB.

8.1.2 Software design

For communication purposes, the PCB with temperature sensors was connected to PC using a USB-MPSSE connector with the ability to provide USB to I^2C interface. The software for communication was developed using Python 3.6 language. At first, the software initializes communication between master and slaves, i.e. PC and temperature sensors TMP100 and TMP461. The communication frequency is set to 100 kHz since this value is suitable for both temperature sensors and is appropriate in terms of length of connection wires used for the

experiment. Furthermore, measurement start time and date are added to the beginning of each log along with titles for each column of measurement. Afterwards, a command for temperature read-out is sent to each slave. Subsequently, received data are converted to temperature in Celsius scale according to the datasheet. The converted temperature is recorded in the data log along with the time of each measurement. For practical reasons, the current sensed temperature is printed to workspace each cycle. The temperature read-out part of the script for both sensors runs in a while loop until it is terminated by the user. A sample of the code is in Figure 38.

```
1
2   from pyftdi.i2c import I2cController
3   import time
4   import datetime
5
6   # start time of initialization:
7   start_time_init = time.time()
8
9   # i2c config:
10  i2c = I2cController()
11  i2c.configure('ftdi:///1', frequency=100000)
12
13  cTemp_100 = []
14  cTemp_461 = []
15  cTemp_461_1V8 = []
16  cTemp_112 = []
17
18  # text file:
19  file = open("testing_#1","w")
20  file.write("#start of measurement:\n")
21  file.write("#%s\n" % datetime.datetime.now())
22  file.write("#time[s] TMP100[C] TMP461[C]\n")
23  start_time = time.time()
24
25  while True:
26
27      ##################################################################
28      # tmp461 - address 0x4E
29      slave_461 = i2c.get_port(0x4E)
30      # uncomment for configuration editing:
31      # slave_461.write_to(0x09, b'\x00')
32      # slave_461.write_to(0x16, b'\x01')
33      time.sleep(0.2)
34      data_461_0 = slave_461.read_from(0x00, 1)
35      data_461_1 = slave_461.read_from(0x15, 1)
36      # temp calc.:
37      temp_461 = (data_461_0[0] * 256 + (data_461_1[0] & 0xF0)) / 16
38      if temp_461 > 2047:
39          temp_461 -= 4096
40      cTemp_461 = temp_461 * 0.0625
41      print("Temperature in Celsius for tmp461 is: %.4f C" % cTemp_461)
```

Figure 38: A sample of the code used to control TMP100 and TMP461. The example shows the I^2C configuration, logging and temperature reading of TMP461.

8.1.3 Experiment design

A bushing with male/female Canon 9-pin connectors on both sides is used as a junction between the inside and the outside of the thermal vacuum chamber. Teflon-coated wires suitable for vacuum conditions were used as a connection between measurement PCB and the Canon 9-pin male connector. Subsequently, PVC-coated wires were used as a connection of the Canon 9-pin female connector and the USB-MPSSE connector since this part of the measurement device is placed outside the thermal vacuum chamber and is not exposed to vacuum conditions. Photo of the measurement setup on top of the cold plate inside the thermal vacuum chamber is in Figure 39. Additionally, for purposes not related to this thesis, a high-voltage power supply and two additional temperature sensors were tested during this experiment.

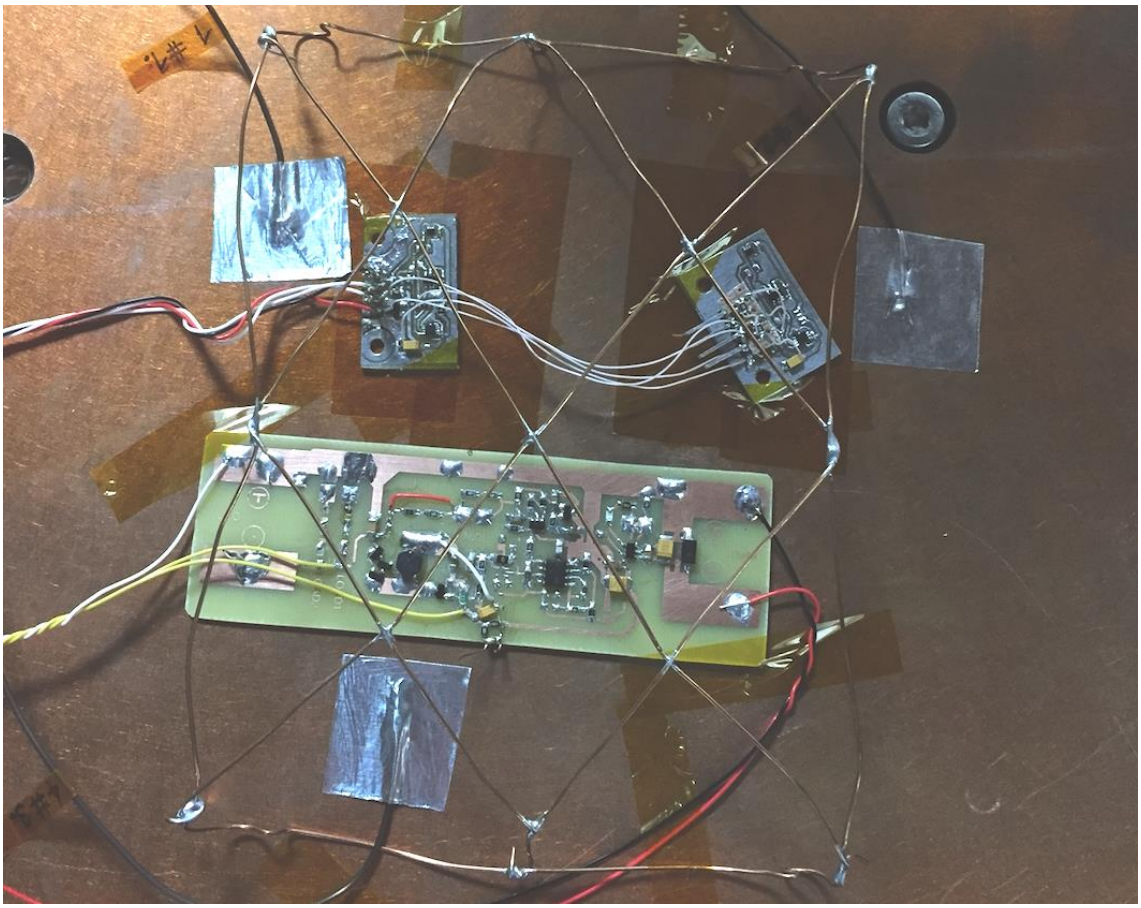

Figure 39: Completed test setup on top of the cold plate inside the thermal vacuum chamber.

For the best possible thermal conduction, the entire PCB was pressed against the cold plate using Kapton tapes. Furthermore, three reference temperature probes were attached to the cold plate in the proximity of the tested equipment using aluminium foil tapes. Furthermore, a copper grid was

attached to the cold plate with Kapton tapes and placed above the setup over which was lately arranged a reflective gold foil. The grid served as a structure ensuring contact-free space between the foil and any conductive parts of the PCB.

Exactly four measurements were planned. At first, sensors were compared while vacuuming the chamber at a constant temperature of approx. 23 °C. After the pressure in the chamber dropped to $4.3 \cdot 10^{-6}$ mBar, three consecutive scenarios were performed, i.e. heating from 23 °C to 81 °C, cooling from 81 °C to -40 °C and heating from -40 °C to 23 °C. For better illustration, the scenarios are described in Table 4.

Table 4: Test scenarios of TMP100 and TMP461 thermal vacuum chamber experiments.

Test number	Temperature range	Pressure range
1	constant at 23 °C	from 1 Bar to $4.3 \cdot 10^{-6}$ mBar
2	from 23 °C to 81 °C	constant at $4.3 \cdot 10^{-6}$
3	from 81°C to -40 °C	constant at $4.3 \cdot 10^{-6}$
4	from -40 °C to 23 °C	constant at $4.3 \cdot 10^{-6}$

8.2 Environmental testing of the XChip pixel detector

Unfortunately, the SpacePix was found to be unable to send proper data even before environmental testing began. As for now, communication with the SpacePix is possible, but the transferred data, i.e. the measured data, were reported to be incorrect. So far, the best estimate is a false operation of the ADC according to SpacePix designers. Since there was no time to wait for a repaired version of the SpacePix, environmental testing of a very similar detector and the SpacePix predecessor, i.e. the XChip pixel detector, was decided instead.

Environmental testing of the XChip detector was conducted in the thermal vacuum chamber through thermal cycling to observe changes in pedestal. Pedestal is subjected to changes depending on the temperature of the XChip. Thus, in terms of histogram representation of the measured data, the width of pedestal peak and location of its mean are a function of temperature and are expected to vary at different temperatures. Therefore, the experiment is conducted in order to investigate changes of the detector's mean and the standard deviation of its pedestal caused by operation at various temperatures in vacuum conditions. Additionally, temperature-based

variations in mean and standard deviation can be utilized for estimation of the temperature-dependent bottom detection limit of the detector.

Pedestal variations can be compared between individual pixels in terms of one image measured at a certain temperature. Consequently, an integral characteristic can be performed. This characteristic examines the dependence of the total energy deposited in all pixels or the dependence of the mean energy deposited on one pixel on the temperature of the detector. Moreover, the number of images obtained at certain temperature should be at least 20 in order to mitigate possible stochastic events. Finally, the tested version of the XChip detector can also be referred to as the XChip telescope since there are two chips stacked on top of each other with the possibility to evaluate the direction of flight of detected particles. Therefore, not one but actually two chips were tested. The XChips are referred to as XChip 1 and XChip 2 within this thesis.

8.2.1 Communication and data log

Communication with the detector is ensured through another PCB potentially usable for other sensors too. This PCB communicates and receives data sent by the XChip detector through the SPI protocol. Afterwards, the received data are packed into packets and sent through UART to the serial port. Not only measured data but also the temperature of the XChip PCB, ID of each XChip detector and the time of measurement is sent along with the data. Finally, the packet is received, deserialized, synchronized and captured data are logged as a binary file. The data are transferred at a rate of 115 200 kbps. Hence, each captured image of approx. 8 kB is transferred in approx. 800 ms. Given that both chips detect at each detection time, the overall data complexity of one image from two chips is approx. 16 kB and the time required for data transfer is approx. 1.6 s.

8.2.2 Thermal cycling design

At first, the temperature range of thermal cycling was determined based on temperatures experienced by internal electronics equipped by LEO satellites. Passive and active thermal control components of spacecraft regulate the interior temperature environment within narrow margins, e.g. 10 °C for a LEO satellite as shown in Figure 40. Even so, electronic components must endure a broader range of temperatures in case of a cold start or an overheat event. Temperature limits

of -10 °C and 55 °C envelope the majority of LEO missions and can serve as a temperature range for thermal testing in the case of an interior component as shown in Figure 40. [52]

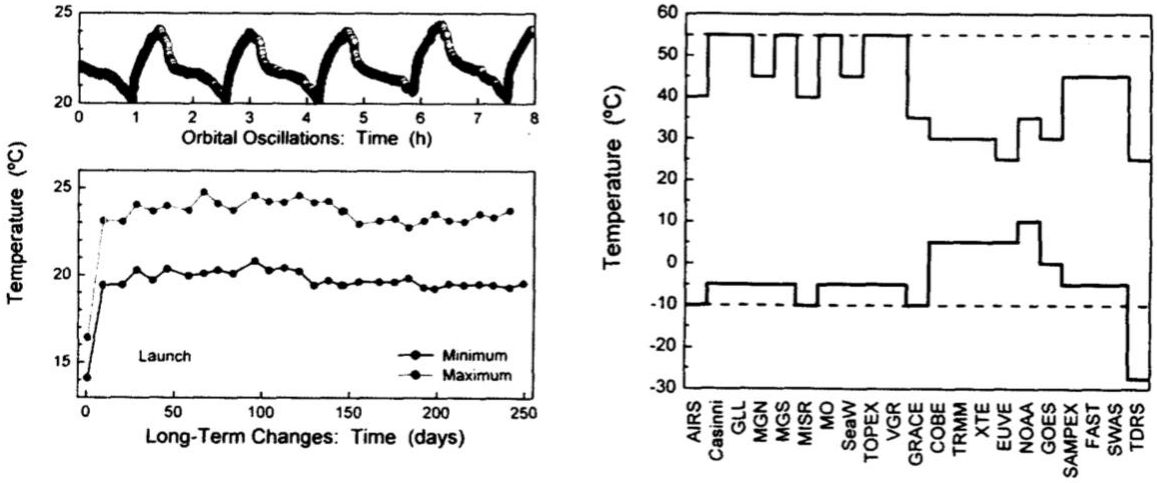

Figure 40: Temperature oscillations on a base plate of a typical LEO spacecraft (left) and extremes experienced by several missions depicted on the horizontal axis (right). All missions are enveloped by the lines of -10 °C and 55 °C except for TDRS orbiting in GEO. [52]

However, a broader temperature range provides more assurance and expands knowledge on electronics limitations. On the other hand, a broader temperature range presents significant increase in experiment time demands. As a compromise, a temperature range of -20 °C to 60 °C was chosen as the thermal cycling range. Figure 41 depicts the M-pattern of the thermal cycle. The first slope is positive and stepping towards the 60 °C limit rather than descending to negative temperatures at first, i.e. forming the W-pattern, and facing the possibility of water vapour condensation and potential damage.

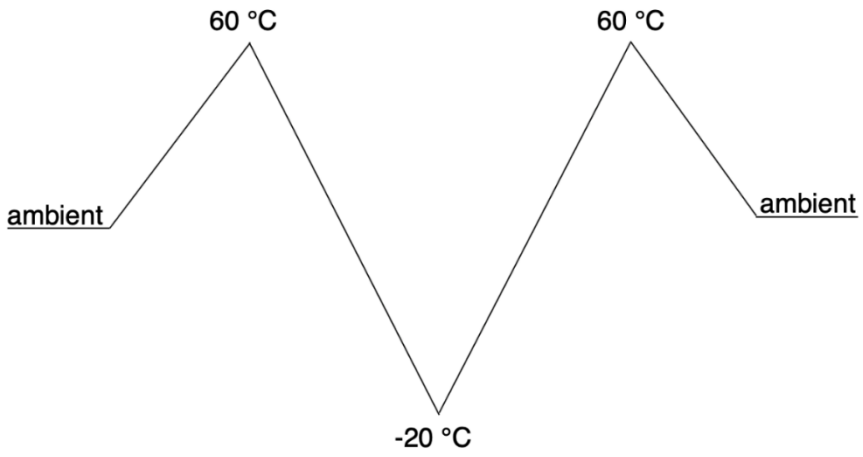

Figure 41: Illustration of the M-pattern of the thermal cycle design.

Furthermore, the pattern is divided by sections of 10 °C into measurement steps, e.g. 30 °C, 40 °C etc., and the detector measures at each step. An example of such step-like layout is presented in Figure 42. This layout assures proper temperature equilibrium between the cold plate of the thermal vacuum chamber and the PCB containing the detector.

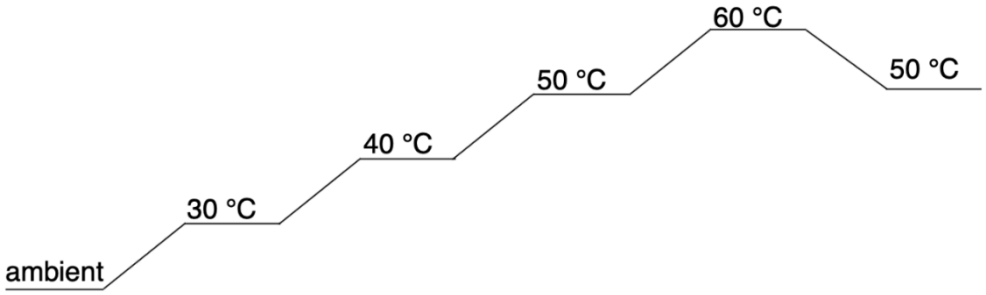

Figure 42: An example of a step-like layout ensuring proper temperature equilibrium between the cold plate of the thermal vacuum chamber and the PCB containing the detector.

However, it is not possible to estimate the accurate time required to achieve the temperature equilibrium between the cold plate and the detector without prior testing. Additionally, the required time varies with dependence on the actual temperature. In the case of the -20 °C temperature step, this time might even be in the order of hours. On the other hand, in the case of the 40 °C temperature step, this time might be in the order of minutes. Therefore, individual temperature steps were reached through increased temperature potential between the cold plate and the detector based on specific needs of each step and in the best possible manner in terms of the temperature deviation and time demands while trying to preserve the original step-like layout. Finally, the time to capture the desired number of images, i.e. 30 images, on each temperature was approx. 48 seconds.

8.2.3 Experiment setup

The connection with the XChip was established through a bushing with male/female Canon 9-pin connectors as in the previous experiment. Also, Teflon-coated wires and PVC-coated wires were used in the same manner as in the previous experiment. The measurement setup placed on top of the cold plate inside the thermal vacuum chamber is in Figure 43.

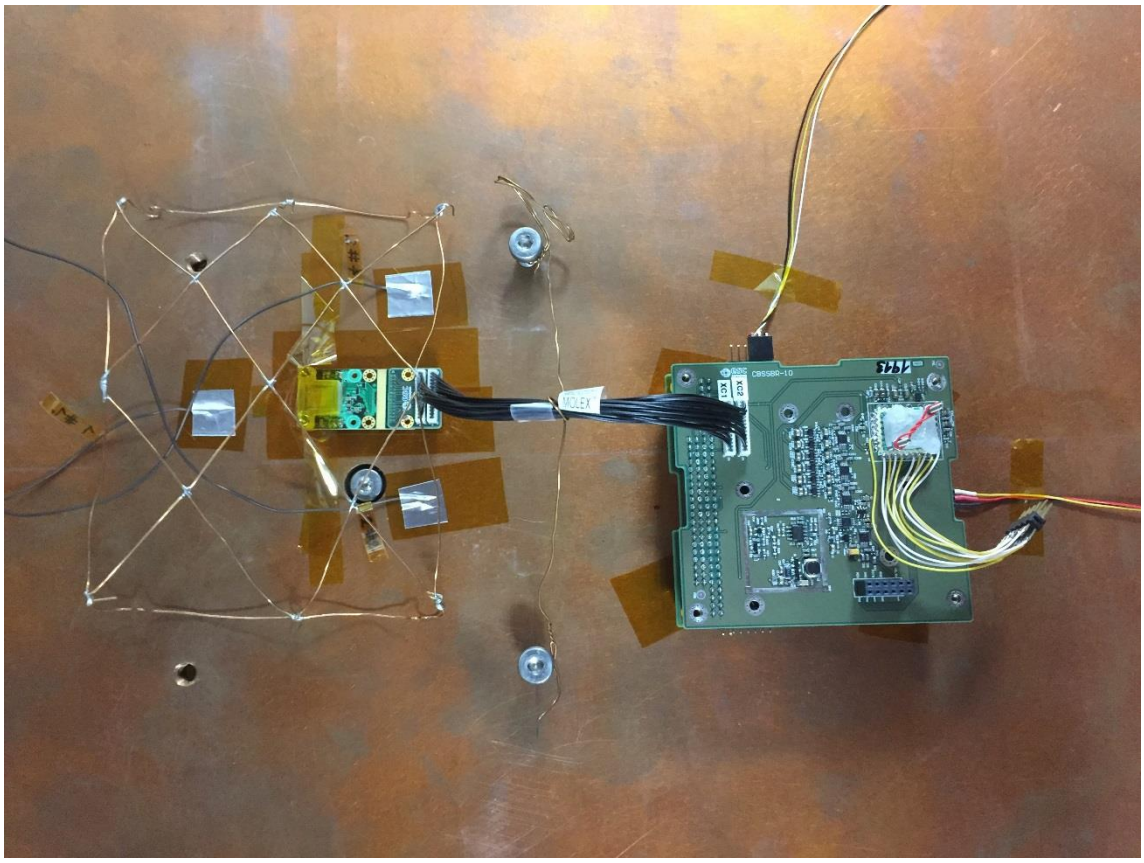

Figure 43: The XChip test setup, i.e. the XChip PCB (left) and the communication PCB (right), on top of the cold plate inside the thermal vacuum chamber.

The thermal junction was established through metal screws used for the XChip docking on the XChip PCB. To avoid any possible shortcuts, the screws and feet of the communication PCB were isolated from the cold plate using Kapton tapes. Kapton tapes also served as a pressure force on the PCB containing the XChip detector to ensure proper connection between the cold plate and the screws. Connection wires between the XChip PCB and the communication PCB were immobilized by a wrapped wire attached to the cold plate. Three temperature probes were added around the XChip PCB to provide reference temperatures of the cold plate. Furthermore, a copper grid was attached to the cold plate using Kapton tapes and placed above the XChip PCB. Over this grid was later arranged a reflective gold foil. The grid's purpose is to ensure contact-free space above the XChip PCB. The temperature of the XChip PCB was measured with TMP461. The pressure in the thermal vacuum chamber was $4.3 \cdot 10^{-6}$ mBar throughout the entire experiment. The XChip was in the ADC mode.

9 Results

9.1 TMP100 and TMP461 vacuum-compatibility testing

Both sensors were tested in the thermal vacuum chamber according to the testing scenarios described in chapter 8.1.3 and Table 4. The outcomes of the testing are shown in Figure 44.

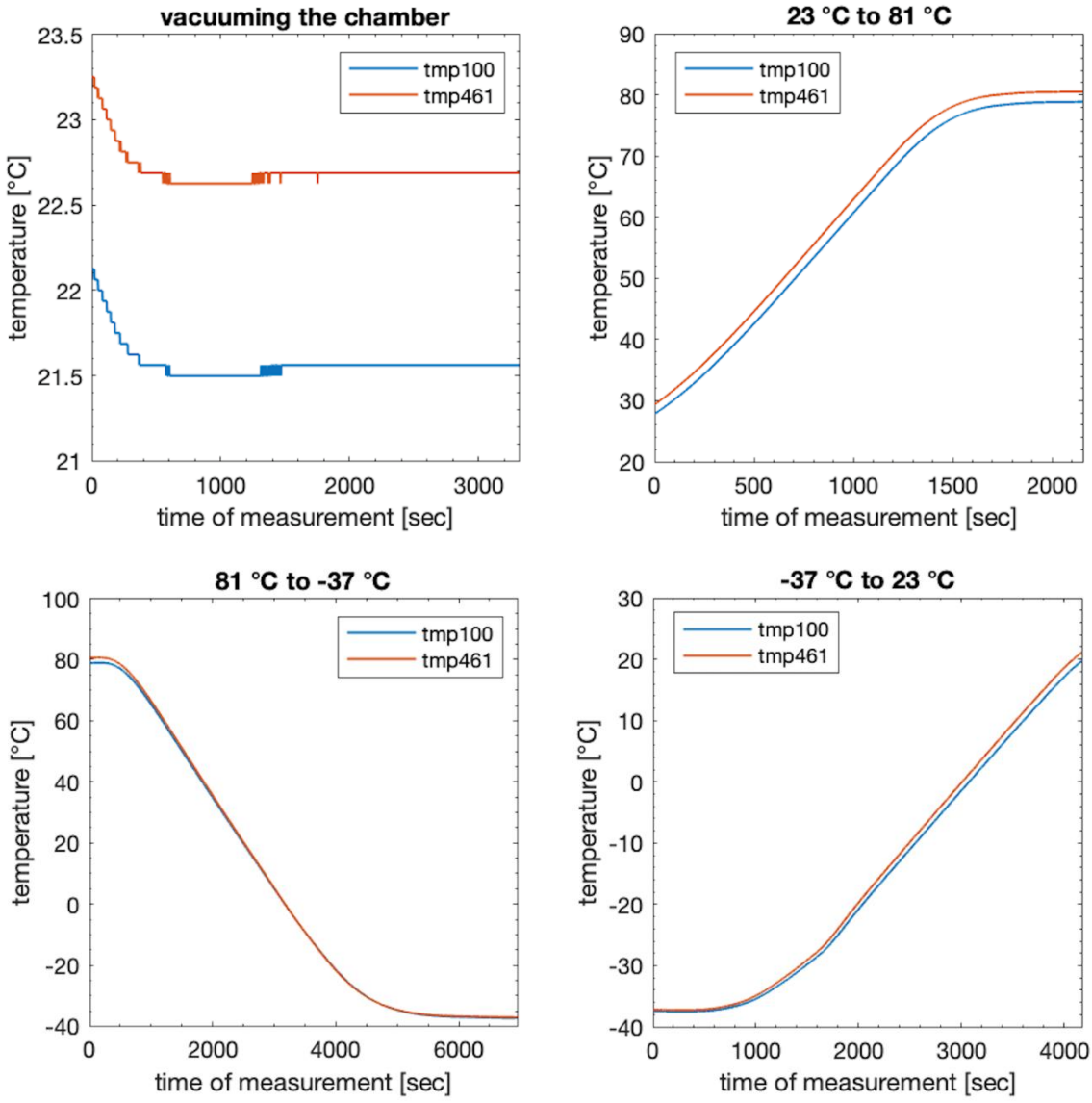

Figure 44: Graphical representation of the results from testing TMP100 and TMP461 temperature sensors. The upper left figure illustrates vacuuming the thermal vacuum chamber at constant temperature, the upper right figure illustrates heating from room temperature to 81 °C in vacuum conditions. The lower left figure illustrates cooling from 81 °C to -37 °C and the lower right figure illustrates heating from -37 °C to room temperature in vacuum conditions.

9.2 XChip environmental testing

Both XChips were tested in the thermal vacuum chamber through thermal cycling detailed in chapter 8.2.2. Exactly 30 measurements were performed at each temperature step for each XChip. Consequently, the 30 obtained matrices of data from every temperature step were averaged resulting in an average matrix of data for each temperature step. The averaged data were further processed.

An example of images reconstructed from data measurement of XChip 1 and XChip 2 obtained at limit temperatures is in Figure 45.

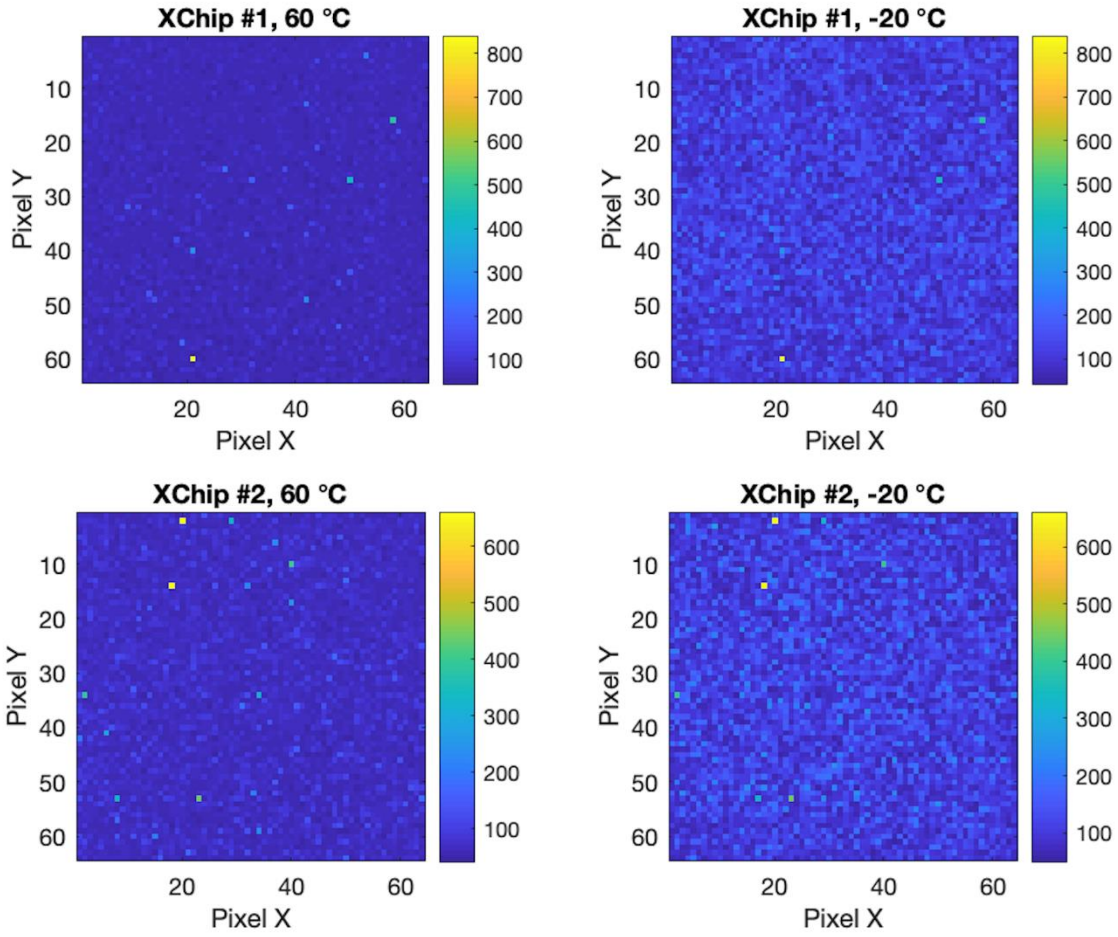

Figure 45: Images reconstructed from XChip 1 (top) and XChip 2 (bottom) measurement. The images on the left side are reconstructed from measurement at 60 °C. The images on the right side are reconstructed from measurement at -20 °C. The colorbars are representing pixel ADC value. The yellow pixel in the bottom left part of XChip 1 images, as well as yellow pixels in the upper left part of XChip 2 images are dead pixels.

Furthermore, histograms representing the distribution of values from individual pixels at limit temperatures from both XChips are shown in Figure 46.

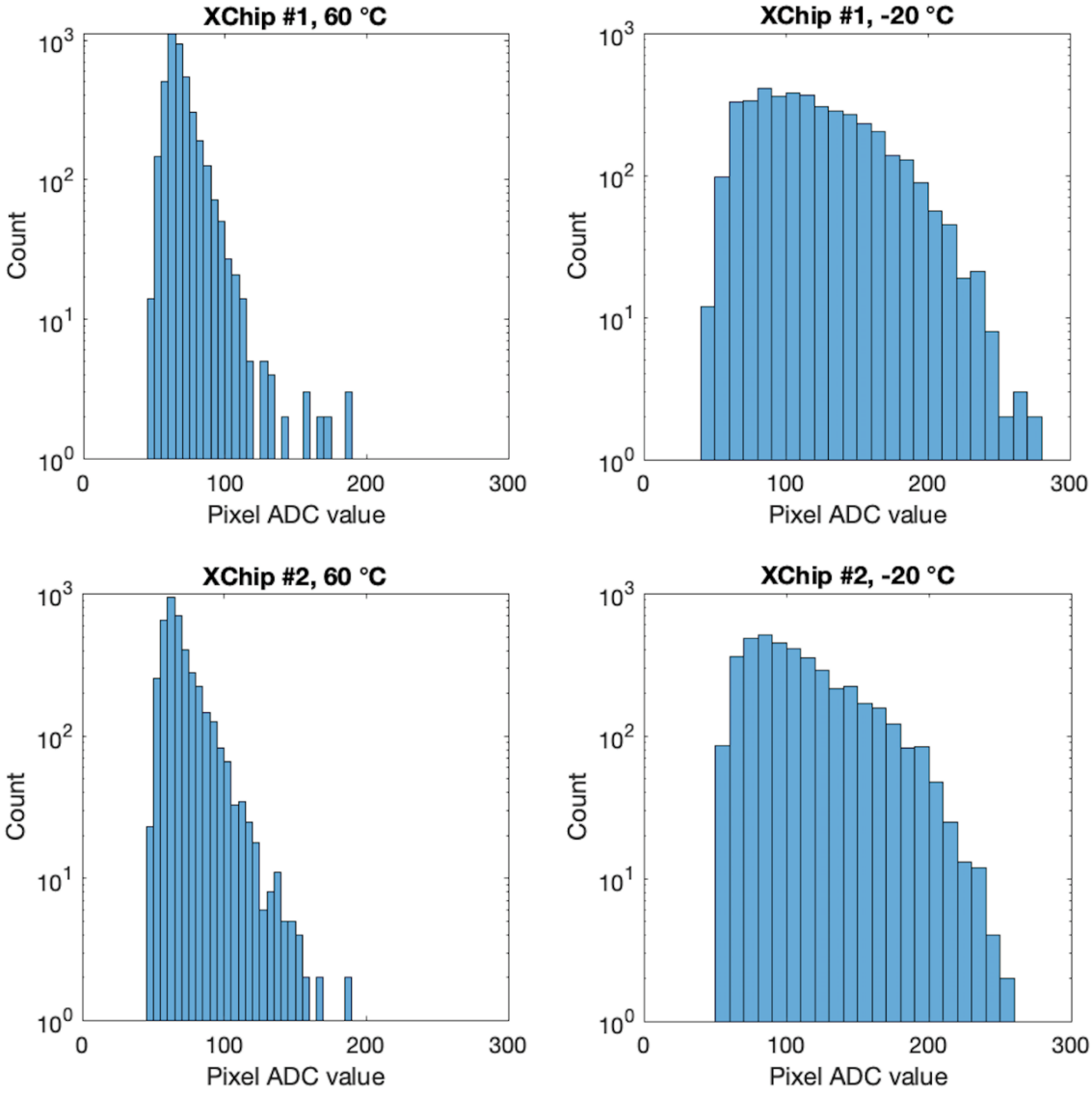

Figure 46: Histograms reconstructed from XChip 1 (top) and XChip 2 (bottom) measurement. The histograms on the left side are reconstructed from measurement at 60 °C. the histograms on the right side are reconstructed from measurement at -20 °C.

Moreover, an integral characteristic of the measured data was performed. Figure 47 depicts the total measured energy in ADC values detected by both XChips as a function of temperature. Similarly, Figure 48 depicts the mean energy of pedestal as a function of temperature along with a 99 % confidence interval.

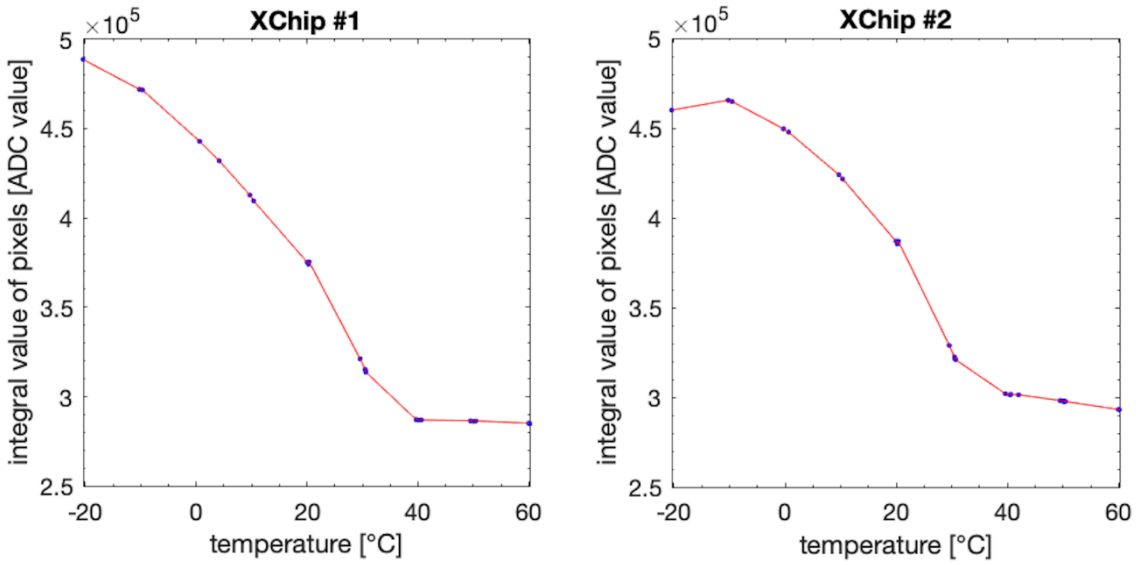

Figure 47: The total energy deposited in all pixels of XChip 1 (left) and XChip 2 (right) as a function of temperature. Blue dots in both figures depict resulting data, red line outlines the trend.

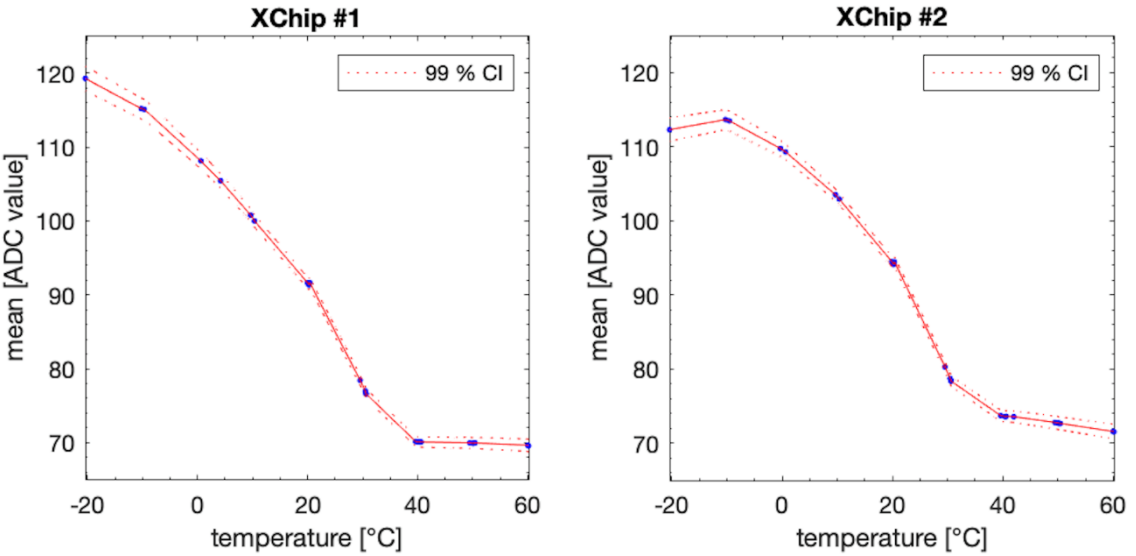

Figure 48: The mean energy deposited on one pixel of XChip 1 (left) and XChip 2 (right) as a function of temperature. Blue dots in both figures depict resulting data, red line outlines the trend. The area between dotted lines represents a 99 % confidence interval of mean values.

Consequently, pedestal variations between individual pixels, i.e. the difference in detected energy of individual pixels, were analysed. These variations were interpreted as the standard deviation of all pixels from an image with regard to the image's mean. Figure 49 illustrates the standard deviation of measured data as a function of temperature.

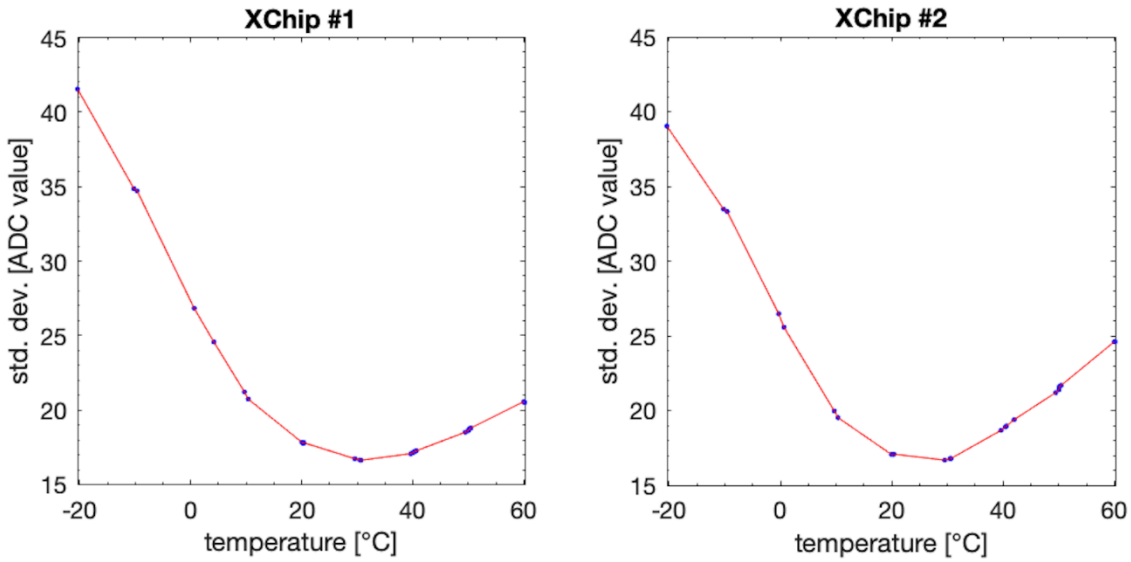

Figure 49: The standard deviation of XChip 1 (left) and XChip 2 (right) measurements as a function of temperature. Blue dots in both figures depict resulting data, red line outlines the trend.

Finally, the temperature-dependent bottom detection limit of both XChips was determined as a sum of the temperature-dependent mean and its upper limit of the 99 % confidence interval. Consequently, 6th-degree polynomials were fitted on the result. Resulting polynomials of both XChips are presented in Table 5. The detection limit is depicted in Figure 50.

Table 5: Bottom detection limit polynomials of both XChips.

XChip	6th-degree polynomial
1	$y = -1.1 \cdot 10^{-8}x^6 + 1.1 \cdot 10^{-6}x^5 - 1.8 \cdot 10^{-5}x^4 - 5.8 \cdot 10^{-4}x^3 + 1.5 \cdot 10^{-3}x^2 - 0.68x + 110$
2	$y = -8.5 \cdot 10^{-9}x^6 + 7.7 \cdot 10^{-7}x^5 - 6.2 \cdot 10^{-6}x^4 - 3.9 \cdot 10^{-4}x^3 - 1.4 \cdot 10^{-2}x^2 - 0.48x + 110$

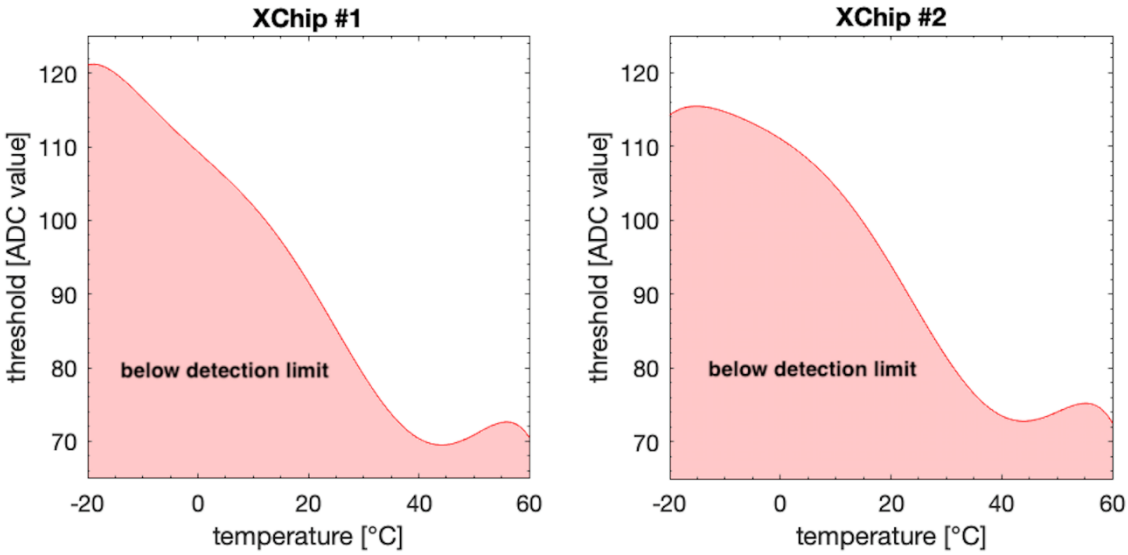

Figure 50: The bottom detection limit of XChip 1 (left) and XChip 2 (right) in terms of the detection threshold as a function of temperature. The highlighted area below the curve represents a region with pedestal dominance.

10 Conclusion

10.1 TMP100 and TMP461 vacuum-compatibility testing

At first, temperature sensors TMP100 and space-hardened TMP461 were subjected to thermal cycling in the thermal vacuum chamber in order to compare their functionality in vacuum conditions. This experiment was conducted a priori to ensure proper temperature measurement of the PCB containing both XChips since it was previously observed that TMP100 performs read-out fluctuations. The result of this experiment is in chapter 9.1 in Figure 44.

All four scenarios were measured as stated in Table 4. Firstly, both sensors measured temperature during the pressure drop inside the thermal vacuum chamber. As the pressure drops, the temperature began to vary in tenths of °C due to changes in mechanical tension experienced by the chip itself and its package. Consequently, both temperature sensors experienced thermal cycling limited by -37 °C and 81 °C. The slope of the temperature change detected by the sensors is similar. Moreover, the absolute temperature difference sensed by both sensors is in tolerance of their reported accuracy which is ±1 °C and ±2 °C for TMP100 and TMP461, respectively. In conclusion, both temperature sensors were determined to measure appropriately in vacuum conditions and both were usable in the environmental testing of the XChip. The reason behind the previously experienced fluctuations of TMP100 remained unclear. A possible explanation is the use of defective TMP100, errors in data transmission or processing, etc.

10.2 XChip environmental testing

Both XChips underwent thermal cycling tests as detailed in chapter 8.2.2 in order to investigate changes in the pedestal of both chips. The pedestal was subjected to variations since it is dependent on temperature. Therefore, the measured data were processed and further analysed in terms of the mean value of the pedestal and its standard deviation as a function of the temperature experienced by the chips. Consequently, the results were utilized in order to determine the bottom detection limit of the chips.

Temperatures of individual measurements were not always as precise as planned and described in chapter 8.2.2. The reason behind this inaccuracy was a combination of the increased temperature potential and occasional desynchronizations leading to consequent failures in data reception. The increased temperature potential, e.g. 4 °C of the cold plate in order to achieve 0 °C

at the XChip PCB, served as a time-saving component throughout the experiment. Random desynchronizations of data reception were caused either by the use of ESA's TASTE operating system through virtual machine or by the communication with XChips through Python. The native application is reported not to have such issues. However, a python script was used rather than the native application due to its versatility such as the possibility to conveniently alter the code according to current measurement needs. Nevertheless, the inaccuracy in measurement at the precise temperatures does not present any problem since it only means denser sampling in terms of evaluated temperature-dependent variables, such as the mean of the pedestal, the integral value of the pedestal and the standard deviation of the pedestal. The results of environmental testing of both XChips are illustrated in chapter 9.2.

At first, an example of images reconstructed from both XChips at limit temperatures, i.e. -20 °C and 60 °C, is in Figure 45. Both XChips detected lower ADC values at 60 °C than at -20 °C. Subsequently, histograms in Figure 46 illustrate the change of the pedestal experienced by XChips at the same limit temperatures. Pixel ADC values along with the standard deviation vary significantly at limit temperatures.

The amount of pedestal change is further detailed. Figure 47 and Figure 48 demonstrate changes in the integral value, i.e. the sum of detected ADC values by all pixels during one exposition, and the mean value of the pedestal as a function of temperature, respectively. Figure 48 also depicts the 99 % confidence interval of the pedestal mean. It was discovered that temperature affects the pedestal in exactly opposite fashion than was assumed. XChips measured lower ADC values of the pedestal at higher temperatures and vice versa. This phenomenon can also be observed in the example images in Figure 45, as well as in the histograms in Figure 46. The reason behind the temperature dependency of the XChip is the temperature dependency of MOSFETs, such as temperature dependency of the threshold voltage and temperature dependency of the electron-hole mobility. These effects alter the output voltage of the current sense amplifier as much as in tens of mV. Other temperature-dependent components are the peak detector hold and the ADC. The resulting temperature dependency of both XChips is the combination of all the aspects described above. Furthermore, Figure 49 demonstrates the pedestal variations between individual pixels in terms of one image as a change of the standard deviation dependent on temperature. The trend of the standard deviation development for both XChips, i.e. higher standard deviation for lower temperatures and vice versa, relates to the same phenomenon as in the case of the mean and the integral value of the pedestal.

Finally, as the outcome of the 99 % confidence interval determination, the bottom detection limit in terms of ADC values was established for both XChips. The resulting data, i.e. the sum of the

means and the upper limit of the 99 % confidence interval, were fitted with 6^{th}-degree polynomials. Both polynomials are presented in Table 5. Moreover, the graphical representation is in Figure 50. Hypothetical irradiation of the detector leading to ADC values below the curve in Figure 50 could not be distinguished from the pedestal values. Therefore, the area below the bottom detection curve is referred to as the region with pedestal dominance and the curve itself as the temperature-dependent bottom detection threshold.

10.3 Further steps and suggestions

In order to transfer measured ADC values to actually detected energy, XChips need to be calibrated. The calibration and known transfer function can also subsequently serve to determine the real bottom detection limit in terms of energy.

Moreover, the power consumption of the XChip is another variable dependent on temperature. Therefore, another step might be determining the temperature characteristic of XChips power consumption. Further steps might also include measurement in a broader range of temperatures since the curves in Figure 47 and 48 indicate further development of the trend in the opposite direction at the limit temperatures. Furthermore, in order to determine a more precise detection limit curve, measurements could be conducted at more temperatures or continuously through thermal cycling. However, a broader range or measurement at more temperatures would present significantly higher time and data complexity demands and might not be considerably beneficial in the case of LEO application.

Finally, experiments with irradiation should be conducted in order to investigate radiation detection properties of the XChip at various temperatures. For instance, suitable radiation sources might include plutonium-238 or characteristic X-rays of copper and germanium. These sources would produce distinguishable peaks at specific energy. Consequently, detected peaks measured at different temperatures can be compared and evaluated in terms of the energy of their mean values and peak widths as in the case of pedestal analyses.

11 References:

[1] Krane, Kenneth S., and David Halliday. *Introductory nuclear physics*. 1987.

[2] Švec, Jiří. "Radioaktivita a ionizující záření." *Ostrava: Vysoká škola báňská* (2005).

[3] Wirawan, Rahadi, et al. "Simulation of energy absorption spectrum in NaI crystal detector for multiple gamma energy using Monte Carlo method." *AIP Conference Proceedings*. Vol. 1656. No. 1. AIP Publishing, 2015.

[4] National Academies of Sciences, Engineering, and Medicine. 2018. *Testing at the Speed of Light: The State of U.S. Electronic Parts Space Radiation Testing Infrastructure*. Washington, DC: The National Academies Press. https://doi.org/10.17226/24993.

[5] Townsend, Lawrence W. "Implications of the space radiation environment for human exploration in deep space." *Radiation protection dosimetry* 115.1-4 (2005): 44-50.

[6] Shapiro, Maurice M., ed. *Composition and origin of cosmic rays*. Vol. 107. Springer Science & Business Media, 2012.

[7] Pissarenko, N. F. Radiation environment during the long space mission (Mars) due to galactic cosmic rays. In: Proceedings of a NATO Advanced Study Institute on Biological Effects and Physics of Solar and Galactic Cosmic Radiation, Part B. Swenberg, C. E., Horneck, G. and Stassinopoulos, E. G., Eds. Series A, Vol. 243B, pp. 1–15 (1993), Plenum Press, New York.

[8] Reames, Donald V. "Solar energetic particles: A paradigm shift." *Reviews of Geophysics* 33.S1 (1995): 585-589.

[9] Horne, Richard B., et al. "Wave acceleration of electrons in the Van Allen radiation belts." *Nature* 437.7056 (2005): 227.

[10] Tan, Yue Chuan, et al. "Silicon avalanche photodiode operation and lifetime analysis for small satellites." *Optics express* 21.14 (2013): 16946-16954.

[11] Mikaelian, Tsoline. "Spacecraft charging and hazards to electronics in space." *arXiv preprint arXiv:0906.3884* (2009).

[12] Srour, Joseph R., and James M. McGarrity. "Radiation effects on microelectronics in space." *Proceedings of the IEEE* 76.11 (1988): 1443-1469.

[13] Stephen, James H. "Hazards to electronics in space." *The behavior of systems in the space environment*. Springer, Dordrecht, 1993. 407-435.

[14] Kolasinski, W. A., Effects of Space Radiation on Electronic Microcircuits, in NASA/SDIO Space Environmental Effects on Materials Workshop, NASA CP-3035, Part 2, pp. 383-392, 1989.

[15] Liemohn, H., Single Event Upset of Spacecraft Electronics, Proc. of Spacecraft Anomalies Conference, NOAA, October 1984.

[16] *SINGLE EVENT UPSET FOR UOSAT-3 S/C*. ESA, 1991. Available from: http://www.esa.int/spaceinimages/Images/2007/03/Single_Event_Upset_for_Uosat-3_spacecraft

[17] Srour, J. R., Cheryl J. Marshall, and Paul W. Marshall. "Review of displacement damage effects in silicon devices." *IEEE Transactions on Nuclear Science* 50.3 (2003): 653-670.

[18] *Walters, R. J., and G. P. Summers. "Space Radiation Effects in Advanced Solar Cell Materials and Devices." MRS Online Proceedings Library Archive 692 (2001).*

[19] Nelson, Gregory A. "Space radiation and human exposures, a primer." Radiation research 185.4 (2016): 349-358.

[20] Protection, Radiological. "ICRP publication 103." *Ann ICRP*37.2.4 (2007): 2.

[21] Cucinotta, Francis A. "Radiation risk acceptability and limitations." *Space Radiation Program Element, NASA Johnson Space Center, Houston, TX* (2010).

[22] Rask, Jon, et al. "Space Faring: The Radiation Challenge." *Nasa, Module* 3.8 (2008): 9.

[23] Hellweg, Christine E., and Christa Baumstark-Khan. "Getting ready for the manned mission to Mars: the astronauts' risk from space radiation." *Naturwissenschaften* 94.7 (2007): 517-526.

[24] Mahesk, K. "Techniques of radiation dosimetry." (1985).

[25] Benton, E. R., and E. V. Benton. "Space radiation dosimetry in low-Earth orbit and beyond." *Nuclear Instruments and Methods in Physics Research Section B: Beam Interactions with Materials and Atoms* 184.1-2 (2001): 255-294.

[26] Hine, Gerald J., and Gordon L. Brownell, eds. *Radiation dosimetry*. Elsevier, 2013.

[27] Knoll, Glenn F. *Radiation detection and measurement*. John Wiley & Sons, 2010.

[28] Seco, Joao, Ben Clasie, and Mike Partridge. "Review on the characteristics of radiation detectors for dosimetry and imaging." *Physics in Medicine & Biology* 59.20 (2014): R303.

[29] Kulp W.D. (2013) Ionizing Radiation Detectors. In: Tsoulfanidis N. (eds) Nuclear Energy. Springer, New York, NY

[30] Loveland, Walter D., David J. Morrissey, and Glenn T. Seaborg. *Modern nuclear chemistry*. John Wiley & Sons, 2017.

[31] Lutz, Gerhard. *Semiconductor radiation detectors*. Vol. 40. Berlin: Springer, 1999.

[32] Bednarski, Tomasz, et al. "Calibration of photomultipliers gain used in the J-PET detector." *Bio-Algorithms and Med-Systems* 10.1 (2014): 13-17.

[33] Rossi, Leonardo, et al. *Pixel detectors: From fundamentals to applications*. Springer Science & Business Media, 2006.

[34] Ballabriga, Rafael, Michael Campbell, and Xavier Llopart. "Asic developments for radiation imaging applications: The medipix and timepix family." *Nuclear Instruments and Methods in Physics Research Section A: Accelerators, Spectrometers, Detectors and Associated Equipment* 878 (2018): 10-23.

[35] Kroupa, Martin, et al. "A semiconductor radiation imaging pixel detector for space radiation dosimetry." *Life sciences in space research* 6 (2015): 69-78.

[36] Trojanova, E., et al. "Tissue sensitive imaging and tomography without contrast agents for small animals with Timepix based detectors." *Journal of Instrumentation* 12.01 (2017): C01056.

[37] HAVRÁNEK, M. a Z. JANOSKA. Documentation of the integrated circuit SpacePix. FJFI CAPADS, 2018.
[38] HAVRÁNEK, M. Design documentation of the integrated circuit X-CHIP-03. FJFI CAPADS, 2018.
[39] Vrba, V., et al. "The SpacePix-D radiation monitor technology demonstrator." *Journal of Instrumentation* 13.12 (2018): C12017.
[40] FINCKENOR, Miria M. a Kim K. DE GROH. A Researcher's Guide to Space Environmental Effects: ISS Researcher's Guide Series [online]. National Aeronautics and Space Administration, 2017 [cit. 2019-04-14]. Dostupné z: https://www.nasa.gov
[41] Bertrand, Reinhold. "Conceptual design and flight simulation of space stations." *Aerospace science and technology* 5.2 (2001): 147-163.
[42] Zwiener, J. M. "Thermal Vacuum Bakeout Specification for Contamination Sensitive Hardware." (1986).
[43] Dooling, D., and M. M. Finckenor. "Material selection guidelines to limit atomic oxygen effects on spacecraft surfaces." (1999).
[44] GUSTETIC, Jennifer L. Spacecraft Thermal Protection Systems (TPS) Based on Polybenzoxazole (PBO) With Unique UV, Atomic-O and Solar Wind Protective Coatings. In: NASA's Open Data Portal. 2018.
[45] Garrett, Henry B., and Albert C. Whittlesey. *Guide to mitigating spacecraft charging effects*. John Wiley & Sons, 2012.
[46] Kauder, Lonny. "Spacecraft thermal control coatings references." (2005).
[47] Silverman, Edward M. "Space environmental effects on spacecraft: LEO materials selection guide, part 1." (1995).
[48] Lai, Shu T., Edmond Murad, and William J. McNeil. "Hazards of hypervelocity impacts on spacecraft." *Journal of Spacecraft and Rockets* 39.1 (2002): 106-114.
[49] Smirnov, N. N., et al. "Space traffic hazards from orbital debris mitigation strategies." *Acta Astronautica* 109 (2015): 144-152.
[50] Poivey, Christian, and John H. Day. "Radiation hardness assurance for space systems." (2002).
[51] Velazco, Raoul, Pascal Fouillat, and Ricardo Reis, eds. *Radiation effects on embedded systems*. Springer Science & Business Media, 2007.
[52] Petkov, Mihail P. "The effects of space environments on electronic components." (2003).
[53] Yu, Fa-Xin, et al. "Overview of Radiation Hardening Techniques for 1C Design." *Information Technology Journal* 9.6 (2010): 1068-1080.
[54] Vukic, V., and P. Osmokrovic. "Total ionizing dose response of commercial process for synthesis of linear bipolar integrated circuits." *Journal of Optoelectronics and Advanced Materials* 8.4 (2006): 1538-1544.

[55] Hafer, Craig, et al. "Next generation radiation-hardened SRAM for space applications." *2006 IEEE Aerospace Conference*. IEEE, 2006.

[56] Yoshikawa, Akihiko, Hiroyuki Matsunami, and Yasushi Nanishi. "Development and applications of wide bandgap semiconductors." *Wide Bandgap Semiconductors*. Springer, Berlin, Heidelberg, 2007. 1-24.

[57] Kern, Werner, and Ronald K. Smeltzer. "BOROPHOSPHOSILICATE GLASSES FOR INTEGRATED-CIRCUITS." *Solid State Technology* 28.6 (1985): 171-179.

[58] Trivedi, Rakesh, and Usha S. Mehta. "A survey of radiation hardening by design (rhbd) techniques for electronic systems for space application." *International Journal of Electronics and Communication Engineering & Technology (IJECET)* 7.1 (2016): 75.

[59] Sinclair, Doug, and Jonathan Dyer. "Radiation effects and COTS parts in SmallSats." (2013).

[60] Todd, B., and S. Uznanski. "Radiation risks and mitigation in electronic systems." *arXiv preprint arXiv:1607.01573* (2016).